Craya decomposition using compactly supported biorthogonal wavelets

Erwan Deriaz, Marie Farge, Kai Schneider

Preprint accepted for publication in Applied and Computational Harmonic Analysis, Special Issue on Continuous Wavelet Transform in Memory of Jean Morlet

Craya decomposition using compactly supported biorthogonal wavelets

Erwan Deriaz*†, Marie Farge† and Kai Schneider*‡

February 26, 2010

Abstract

We present a new local Craya–Herring decomposition of three-dimensional vector fields using compactly supported biorthogonal wavelets. Therewith vector-valued function spaces are split into two orthogonal components, i.e., curl-free and divergence-free spaces. The latter is further decomposed into toroidal and poloidal parts to decorrelate horizontal from vertical contributions which are of particular interest in geophysical turbulence. Applications are shown for isotropic, rotating and stratified turbulent flows. A comparison between isotropic and anisotropic orthogonal Craya–Herring wavelets, built in Fourier space and thus not compactly supported, is also given.

Keywords: Craya-Herring decomposition, divergence-free wavelets, stratified flows, wave-vortex expansion.

1 Introduction

Stratified and rotating flows are generic situations encountered in geophysical turbulence, e.g. the jet-stream in the tropopause, e.g. [26]. Modeling and computing of such flows is typically based on the three-dimensional Navier–Stokes equations coupled with a heat equation using the Boussinesq approximation. The spatial variations of density are only considered as a source of buoyancy force and thus the velocity field remains divergence-free. The presence of stratification and rotation induces some anisotropy, which is directly reflected by the topology of coherent vortical structures observed in nature and in numerical experiments. For example, in rotating flows elongated vertical structures (vortex tubes) are present, while in the stratified case flattened horizontal structures (pancakes) are found [24, 2]. A concise presentation can be found in the book by Sagaut and Cambon [28], as well as a detailed survey of applications of Craya decomposition and its variants to turbulent flows, both incompressible and compressible.

The Craya basis [7] has been introduced in the fifties in the the context of the statistical description of anisotropic homogeneous turbulence. Later Herring [17] has applied

*Laboratoire de Mécanique, Modélisation et Procédés Propres, UMR 6181 CNRS, 38 rue Frédéric Joliot-Curie 13451 Marseille Cedex 20 (France), ederiaz@L3M.univ-mrs.fr

†LMD-IPSL-CNRS, École Normale Supérieure, 24 rue Lhomond 75231 Paris, cedex 05 (France), farge@lmd.ens.fr

‡Centre de Mathématiques et d'Informatique, Université de Provence, 39 rue Frédéric Joliot-Curie, 13453 Marseille Cedex 13 (France), kschneid@cmi.univ-mrs.fr

the Craya decomposition to turbulent fluctuations and studied the return to isotropy of axisymmetric turbulence. First applications of the Craya decomposition to the dynamics of turbulent fluctuations can be found in Cambon et al. [5]. Cambon and co-workers introduced the Craya decomposition to study geophysical turbulence in spectral space [15, 3]. They stressed the link of the Craya decomposition to the "wave-vortex" decomposition by Riley et al. [27] in physical space, clarifying its toroidal-poloidal type. A variant of the Craya decomposition is the "helical mode" decomposition, introduced by Cambon & Jacquin [4] for studying the dynamics of rotating turbulence, and used also by Waleffe for analysing nonlinearity in turbulence with and without rotation [32]. Applications to stratified flows using representation in physical space can be found in [27]. Incompressible turbulent flows can thus be decomposed into a geostrophically balanced component and two unbalanced ones using the linearized Boussinesq equations. This decomposition, also called wave-vortex expansion [32], thus splits the flow into geostrophic vortices and ageostrophic gravity waves. Taking into account the incompressibility, the primitive variables, velocity and temperature, four in total, are replaced by three new variables: the quasi-geostrophic (QG) potential vorticity q, the horizontal divergence χ and the thermal wind imbalance ξ. The first variable corresponds to the flow component in geostrophic balance, while the two other variables characterize the departure from geostrophic and hydrostatic balance. The QG potential vorticity is a scalar field which is transported by the geostrophically balanced horizontal components of the total velocity. For applications of the Craya decomposition to turbulence we refer, e.g., to [5], or to [13], the latter using the wavelet based coherent vortex extraction.

From mathematical point of view the Craya decomposition is based on the Fourier representation of the flow fields which are supposed to be homogeneous, for a review we refer to [28]. The divergence-free constraint of the velocity field is in Fourier space equivalent to the orthogonality of the Fourier modes with respect to the wave vector. This means that the incompressible modes are located in the tangent plane of the unit sphere in wave number space. Introducing a local coordinate system on this unit sphere, using poloidal (latitudinal) and toroidal (longitudinal) coordinates, is the principle to define the Craya modes, as illustrated in [3]. By construction Craya modes are perfectly localized in Fourier space, therefore they are not locally supported in physical space and have a wave-like structure. To overcome the limitation of Craya modes based on the Fourier decomposition we propose to use instead the wavelet decomposition to construct localized modes which we call Crayalets.

Wavelets, introduced by Grossmann & Morlet in 1984 [16], have been applied to analyze turbulent flows since the end of the eighties [14] and early nineties [12, 25]. For a recent review on the use of wavelets for computational fluid dynamics we refer to [29]. The construction of divergence-free wavelets emerged soon after the invention of wavelets. The first construction by Battle and Federbush in 1993 [1] issued in orthogonal divergence-free wavelets. They have exponential decay in physical space and were used to study the existence of solutions of the Navier–Stokes equations. Kishida *et al.* [19] constructed orthogonal divergence-free wavelets in Fourier space. The resulting wavelets are badly localized in physical space as they exhibit algebraic decay only. Applications were dealing with homogeneous turbulence dynamics to study local and non-local interactions [18, 19].

In 1994 Lemarié proved the inexistence of orthogonal divergence-free wavelets with compact support [21]. Thus in order to obtain divergence-free wavelets with compact support one has to relax the orthogonality condition and switch to biorthogonal constructions. In [20] Lemarié constructed compactly supported divergence-free wavelets on $\mathbb{R}^n$ with the

help of biorthogonal multiresolution analysis (MRA). Urban generalized this construction to non-tensorial MRAs [30] and used them to solve numerically the Stokes equation for a driven cavity problem [31]. The introduction of anisotropic biorthogonal divergence-free wavelets in [9], reducing the diversity of needed vector-valued wavelets, simplified the understanding of their construction and their applicability.

A first construction of orthogonal Crayalets directly in Fourier space using the Meyer wavelet for the numerical applications, was proposed in [18]. The resulting Crayalets are orthogonal but not compactly supported. They exhibit a slow decay at infinity, like $O(||x||^{-2})$. The aim of the present paper is to construct compactly supported Crayalets using biorthogonal wavelets. The motivation is to dispose of an efficient algorithm for local Craya–Herring decompositions using the fast wavelet transform and to analyze therewith different types of flows corresponding to isotropic, rotating and stratified turbulence.

The remainder of the paper is organized as follows. First, we recall the Craya decomposition in Fourier space. Then vector-valued wavelets obtained by Fourier transform are presented and the construction of orthogonal Crayalets, originally proposed in [18, 19], is exposed in a mathematically concise way. Different biorthogonal Crayalet bases, constructed directly in physical space, are introduced using similar techniques as those used for the construction of compactly supported biorthogonal wavelets. Visualizations of the orthogonal and biorthogonal Crayalets are shown. A generalization to higher space dimensions is also discussed. Section 4 shows different types of turbulent flows, i.e., isotropic, stratified and rotating turbulence, which are projected and compressed onto these new bases. Their compression properties are studied in detail. Finally, conclusions are drawn and some perspectives for future work are given.

1.1 Craya in the continuity of Helmholtz

The Helmholtz decomposition consists in separating the divergence-free part of a vector-valued field from its gradient part. That means a vector-valued field $\mathbf{u} = (u_1, u_2, u_3)$ can be decomposed into:

$$\mathbf{u} = \mathbf{u}_{\mathrm{div}} + \mathbf{u}_{\mathrm{rot}} \qquad \text{with} \quad \mathbf{u}_{\mathrm{div}} \perp \mathbf{u}_{\mathrm{rot}}$$

with $\operatorname{div} \mathbf{u}_{\mathrm{div}} = 0$ and $\operatorname{rot} \mathbf{u}_{\mathrm{rot}} = 0$. These conditions on $\mathbf{u}_{\mathrm{div}}$ and $\mathbf{u}_{\mathrm{rot}}$ are equivalent to the existence of two functions: a stream function $\boldsymbol{\psi}$ (which is a scalar-valued function in 2D and a divergence-free vector-valued function in 3D) and a scalar potential function p such that $\mathbf{u}_{\mathrm{div}} = \operatorname{rot} \boldsymbol{\psi}$ and $\mathbf{u}_{\mathrm{rot}} = \nabla p$.

The Craya decomposition [7, 19] adds a decomposition on the divergence-free part of the function:

$$\mathbf{u}_{\mathrm{div}} = \mathbf{u}_{\mathrm{T}} + \mathbf{u}_{\mathrm{P}}$$

where $\mathbf{u}_{\mathrm{T}}$ is the toroidal part with no vertical component, and $\mathbf{u}_{\mathrm{P}}$ is the poloidal part which is such that, any two dimensional horizontal extraction of $\mathbf{u}_{\mathrm{P}}$ is a two dimensional gradient function. That means: there exist functions ρ and q such that

$$\mathbf{u}_{\mathrm{T}} = \begin{bmatrix} \partial_2 \rho \\ -\partial_1 \rho \\ 0 \end{bmatrix} \quad \text{and} \quad \mathbf{u}_{\mathrm{P}} = \begin{bmatrix} \partial_1 q \\ \partial_2 q \\ u_{\mathrm{div}\,3} \end{bmatrix}$$

Here, $u_{\mathrm{div}\,3}$ stands for the third component of $\mathbf{u}_{\mathrm{div}}$ and ∂_1 for the derivative with respect to x_1, i.e., $\frac{\partial}{\partial x_1}$.

In terms of the decomposition of function spaces the Helmholtz decomposition yields:

$$(L^2(\mathbb{R}^3))^3 = \mathbf{H}_{\mathrm{div},0}(\mathbb{R}^3) \oplus^{\perp} \mathbf{H}_{\nabla}(\mathbb{R}^3) \tag{1.1}$$

where

$$\mathbf{H}_{\mathrm{div},0}(\mathbb{R}^3) = \{\mathbf{v} \in (L^2(\mathbb{R}^3))^3 \ ; \ \mathrm{div}\ \mathbf{v} \in L^2(\mathbb{R}^3), \quad \mathrm{div}\ \mathbf{v} = 0\}$$

is the space of divergence-free vector-valued functions, and

$$\mathbf{H}_{\nabla}(\mathbb{R}^3) = \{\mathbf{v} \in (L^2(\mathbb{R}^3))^3 \ ; \ \mathrm{curl}\ \mathbf{v} \in (L^2(\mathbb{R}^3))^3, \quad \mathrm{curl}\ \mathbf{v} = 0\}$$

the space of curl-free vector-valued functions. The Craya decomposition splits the former space further into

$$\mathbf{H}_{\mathrm{div},0}(\mathbb{R}^3) = \mathbf{H}_{\mathrm{T}}(\mathbb{R}^3) \oplus^{\perp} \mathbf{H}_{\mathrm{P}}(\mathbb{R}^3),$$

where

$$\mathbf{H}_{\mathrm{T}}(\mathbb{R}^3) = \{\mathbf{v} = (v_1, v_2, v_3) \in \mathbf{H}_{\mathrm{div},0}(\mathbb{R}^3), \quad v_3 = 0\}$$

is the space of toroidal functions, and $\mathbf{H}_{\mathrm{P}}(\mathbb{R}^3)$ the orthogonal complement space of $\mathbf{H}_{\mathrm{T}}(\mathbb{R}^3)$ in $\mathbf{H}_{\mathrm{div},0}(\mathbb{R}^3)$.
This leads to the orthogonal Craya decomposition:

$$(L^2(\mathbb{R}^3))^3 = \mathbf{H}_{\nabla}(\mathbb{R}^3) \oplus^{\perp} \mathbf{H}_{\mathrm{T}}(\mathbb{R}^3) \oplus^{\perp} \mathbf{H}_{\mathrm{P}}(\mathbb{R}^3). \tag{1.2}$$

1.2 Craya in Fourier

In the following, we note the Fourier transform

$$\hat{u}(\xi) = \int_{x \in \mathbb{R}^d} u(x) e^{-i\xi \cdot x}\, dx$$

and by $\mathcal{F}^{-1}$ the inverse Fourier transform, so that $\mathcal{F}^{-1}\hat{u} = u$.

In spectral space, the Helmholtz decomposition reads:

$$\widehat{\mathbf{u}} = \widehat{\mathbb{P}\mathbf{u}} + \widehat{\mathbb{Q}\mathbf{u}}$$

with, in dimension three,

$$\widehat{\mathbb{P}\mathbf{u}} = \left(Id - \frac{1}{|\boldsymbol{\xi}|^2} \begin{bmatrix} \xi_1 \\ \xi_2 \\ \xi_3 \end{bmatrix} \times \begin{bmatrix} \xi_1 & \xi_2 & \xi_3 \end{bmatrix} \right) \widehat{\mathbf{u}}$$

and

$$\widehat{\mathbb{Q}\mathbf{u}} = \frac{1}{|\boldsymbol{\xi}|^2} \begin{bmatrix} \xi_1 \\ \xi_2 \\ \xi_3 \end{bmatrix} \times \begin{bmatrix} \xi_1 & \xi_2 & \xi_3 \end{bmatrix} \widehat{\mathbf{u}} \tag{1.3}$$

with $|\boldsymbol{\xi}|^2 = \sum_{\ell=1}^{3} \xi_\ell^2$.

With the help of the Fourier transform, the decomposition between the horizontal divergence-free functions and its divergence-free orthogonal complement can be written as

$$\widehat{\mathbf{u}} = \widehat{\mathbb{P}_{\mathrm{T}}\mathbf{u}} + \widehat{\mathbb{P}_{\mathrm{P}}\mathbf{u}} + \widehat{\mathbb{Q}\mathbf{u}}$$

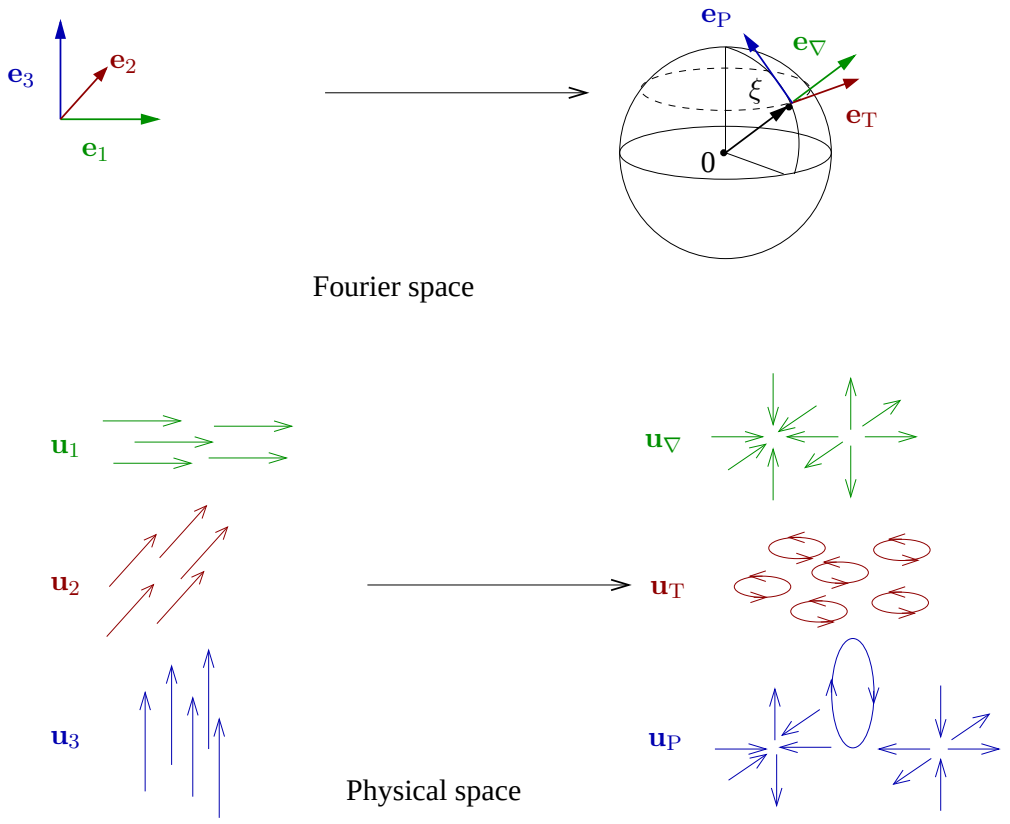

Figure 1: Representation of the three unit vectors ($\mathbf{e}_\nabla$, $\mathbf{e}_\mathrm{T}$ and $\mathbf{e}_\mathrm{P}$) in the Fourier domain (top) and an illustration of the corresponding three manifolds $\mathbf{H}_\nabla$, $\mathbf{H}_\mathrm{T}$, $\mathbf{H}_\mathrm{P}$ (bottom).

where the orthogonal projector $\mathbb{Q}$ is the same as for the Helmholtz decomposition (1.3) and where we write the toroidal projector $\mathbb{P}_\mathrm{T}$ and poloidal projector $\mathbb{P}_\mathrm{P}$:

$$\widehat{\mathbb{P}_\mathrm{T}\mathbf{u}} = \frac{1}{|\boldsymbol{\xi}_h|^2} \begin{bmatrix} \xi_2 \\ -\xi_1 \\ 0 \end{bmatrix} \times \begin{bmatrix} \xi_2 & -\xi_1 & 0 \end{bmatrix} \widehat{\mathbf{u}},$$

$$\widehat{\mathbb{P}_\mathrm{P}\mathbf{u}} = \frac{1}{|\boldsymbol{\xi}_h|^2|\boldsymbol{\xi}|^2} \begin{bmatrix} \xi_1\xi_3 \\ \xi_2\xi_3 \\ -|\boldsymbol{\xi}_h|^2 \end{bmatrix} \times \begin{bmatrix} \xi_1\xi_3 & \xi_2\xi_3 & -|\boldsymbol{\xi}_h|^2 \end{bmatrix} \widehat{\mathbf{u}}$$

using the notation $\boldsymbol{\xi}_h = (\xi_1, \xi_2, 0)$, so that $|\boldsymbol{\xi}_h|^2 = \xi_1^2 + \xi_2^2$.

With the help of the unit vectors

$$\mathbf{e}_\mathrm{T} = \frac{1}{|\boldsymbol{\xi}_h|} \begin{bmatrix} i\xi_2 \\ -i\xi_1 \\ 0 \end{bmatrix}, \quad \mathbf{e}_\mathrm{P} = \frac{1}{|\boldsymbol{\xi}||\boldsymbol{\xi}_h|} \begin{bmatrix} \xi_1\xi_3 \\ \xi_2\xi_3 \\ -|\boldsymbol{\xi}_h|^2 \end{bmatrix}, \quad \text{and} \quad \mathbf{e}_\nabla = \frac{1}{|\boldsymbol{\xi}|} \begin{bmatrix} i\xi_1 \\ i\xi_2 \\ i\xi_3 \end{bmatrix} \tag{1.4}$$

we can write $\widehat{\mathbb{P}_\mathrm{T}\mathbf{u}} = \langle \widehat{\mathbf{u}}, \mathbf{e}_\mathrm{T}^* \rangle \mathbf{e}_\mathrm{T}$, $\widehat{\mathbb{P}_\mathrm{P}\mathbf{u}} = \langle \widehat{\mathbf{u}}, \mathbf{e}_\mathrm{P}^* \rangle \mathbf{e}_\mathrm{P}$, and $\widehat{\mathbb{Q}\mathbf{u}} = \langle \widehat{\mathbf{u}}, \mathbf{e}_\nabla^* \rangle \mathbf{e}_\nabla$ where we noted by a^* the complex conjugate of a.

Notice that $\mathbf{e}_{\mathrm{P}} = -\mathbf{e}_{\nabla} \wedge \mathbf{e}_{\mathrm{T}}$ and $\mathbf{e}_{\mathrm{T}} = \mathbf{e}_{\nabla} \wedge \mathbf{e}_{\mathrm{P}}$. As the operator $\mathbf{e} \mapsto |\boldsymbol{\xi}| \mathbf{e}_{\nabla} \wedge \mathbf{e}$ corresponds in Fourier space to the curl operator in physical space, it means that the curl of a toroidal vector function is poloidal, and vice versa. For a graphical illustration we refer to Fig. 1 (top).

2 Vector-valued wavelets on projected spaces: the general case

In order to understand better the construction of wavelet bases on spaces obtained by Fourier transform and orthogonal projections, we propose to study the general case and describe the properties of the derived wavelets.

Definition 2.1 *Let $\boldsymbol{\varepsilon}_1, \dots, \boldsymbol{\varepsilon}_n : \mathbb{R}^n \to \mathbb{C}^n$ be functions such that*
(i) $\forall \boldsymbol{\xi} \in \mathbb{R}^n$, $(\boldsymbol{\varepsilon}_1(\boldsymbol{\xi}), \dots, \boldsymbol{\varepsilon}_n(\boldsymbol{\xi}))$ *form an orthonormal basis of* $\mathbb{C}^n$,
(ii) $\forall \boldsymbol{\xi} \in \mathbb{R}^n$, $\forall \ell \in \{1, \dots, n\}$, $\boldsymbol{\varepsilon}_\ell(-\boldsymbol{\xi}) = \boldsymbol{\varepsilon}_\ell(\boldsymbol{\xi})^*$.

As a consequence of (i), we have
(iii) $\forall \boldsymbol{\xi} \in \mathbb{R}^n$, $\forall \ell \in \{1, \dots, n\}$, $\|\boldsymbol{\varepsilon}_\ell(\boldsymbol{\xi})\| = 1$, and then
(iv) $\forall f \in L^2(\mathbb{R}^n)$, $\forall \ell \in \{1, \dots, n\}$, $\boldsymbol{\xi} \mapsto f(\boldsymbol{\xi}) \boldsymbol{\varepsilon}_\ell(\boldsymbol{\xi}) \in (L^2(\mathbb{R}^n))^n$.
Assertion (ii) allows to conserve the property $f(-\boldsymbol{\xi}) = f(\boldsymbol{\xi})^*$ which means that if f is the Fourier transform of a real-valued function, then so is $\boldsymbol{\xi} \mapsto f(\boldsymbol{\xi}) \boldsymbol{\varepsilon}_\ell(\boldsymbol{\xi})$. For instance, the functions $\mathbf{e}_{\mathrm{P}}$, $\mathbf{e}_{\nabla}$ and $\mathbf{e}_{\mathrm{T}}$ from equation (1.4) satisfy conditions (i) and (ii).
We are now able to introduce the following vector-valued wavelets:

Definition 2.2 *Let $\{\psi_\lambda\}_{\lambda \in \Lambda}$ be a wavelet basis of $L^2(\mathbb{R}^n)$, then the set of functions*

$$\Psi_{\ell,\lambda} = \mathcal{F}^{-1}(\widehat{\psi_\lambda} \boldsymbol{\varepsilon}_\ell)$$

for $\ell \in \{1, \dots, n\}$ and $\lambda \in \Lambda$ forms an orthogonal real-valued basis of $\left(L^2(\mathbb{R}^n)\right)^n$.

These 'wavelets' do not inherit the properties of the wavelet basis $\{\psi_\lambda\}_\lambda$ automatically. The scale invariance is not conserved in general, especially for anisotropic wavelet bases (with $\mathbf{j} \in \mathbb{Z}^n$). This projection also interferes with the compact support property of the wavelets. But it preserves the number of zero-moments – linked to the behavior of the Fourier transform of the multi-dimensional wavelets near $\mathbf{0}$ – and the regularity of the wavelets – linked to the decay properties of the Fourier transform of the multi-dimensional wavelets for $|\boldsymbol{\xi}| \to +\infty$.

Proposition 2.1 *In definition 2.2, if the wavelet basis $\{\psi_\lambda\}_\lambda$ is shift-invariant then the wavelets $\Psi_{\ell,\lambda}$ are still shift-invariant:*

$$\forall \mathbf{k} \in \mathbb{Z}^n, \quad \forall \ell \in \{1, \dots, n\}, \quad \Psi_{\ell,j,\mathbf{k}}(\mathbf{x}) = \Psi_{\ell,j,\mathbf{0}}(\mathbf{x} - 2^{-j}\mathbf{k}),$$

Proof: For two functions f and g which satisfy for some $\mathbf{k} \in \mathbb{R}^n$, $f(\mathbf{x}) = g(\mathbf{x}+\mathbf{k})$ $\forall \mathbf{x} \in \mathbb{R}^n$, their Fourier transforms are linked by:

$$\hat{f}(\boldsymbol{\xi}) = e^{i\mathbf{k}\cdot\boldsymbol{\xi}} \hat{g}(\boldsymbol{\xi})$$

Hence the multiplication by $\boldsymbol{\varepsilon}_\ell(\boldsymbol{\xi})$ does not change this relation.

Proposition 2.2 *The scale-invariance holds for isotropic wavelets under the condition of homogeneous function on* $\{\varepsilon_\ell\}_{1\leq\ell\leq n}$*:*

$$\forall\lambda\in\mathbb{R}_+^*,\quad \forall\ell\in\{1,\dots,n\},\quad \boldsymbol{\varepsilon}_\ell(\lambda\boldsymbol{\xi})=\boldsymbol{\varepsilon}_\ell(\boldsymbol{\xi}),$$

Proof: For two functions f and g which satisfy for some $\lambda\in\mathbb{R}_+^*$, $f(\mathbf{x})=g(\lambda\mathbf{x})\ \forall\mathbf{x}\in\mathbb{R}^n$, their Fourier transforms are linked by:

$$\hat{f}(\boldsymbol{\xi})=\lambda^{-n}\hat{g}(\lambda^{-1}\boldsymbol{\xi})$$

Hence as $\boldsymbol{\varepsilon}_\ell(\boldsymbol{\xi})\hat{f}(\boldsymbol{\xi})=\lambda^{-n}\boldsymbol{\varepsilon}_\ell(\lambda^{-1}\boldsymbol{\xi})\hat{g}(\lambda^{-1}\boldsymbol{\xi})$, the projected vector-valued wavelet basis is still scale-invariant.

Decomposition on the wavelet basis $\Psi_{\ell,\lambda}$

Suppose $\mathbf{f}\in(L^2(\mathbb{R}^n))^n$. The expansion of $\mathbf{f}$ onto $(\Psi_{\ell,\lambda})_{\ell,\lambda}$ is obtained through the Fourier transform $\mathbf{f}\mapsto\hat{\mathbf{f}}$, and subsequent projection:

$$\hat{\mathbf{f}}(\boldsymbol{\xi})=\sum_{\ell=1}^{n}\langle\hat{\mathbf{f}}(\boldsymbol{\xi}),\boldsymbol{\varepsilon}_\ell(\boldsymbol{\xi})^*\rangle\boldsymbol{\varepsilon}_\ell(\boldsymbol{\xi})$$

Then, for each $\ell\in\{1,\dots,n\}$, we compute the inverse Fourier transform of the function $\hat{f}_\ell:\ \boldsymbol{\xi}\mapsto\langle\hat{\mathbf{f}}(\boldsymbol{\xi}),\boldsymbol{\varepsilon}_\ell(\boldsymbol{\xi})^*\rangle$, $\hat{f}_\ell\mapsto f_\ell$ and we decompose f_ℓ into the wavelet basis $(\psi_\lambda)_\lambda$:

$$f_\ell=\mathcal{F}^{-1}(\langle\hat{\mathbf{f}}(\boldsymbol{\xi}),\boldsymbol{\varepsilon}_\ell(\boldsymbol{\xi})^*\rangle)=\sum_\lambda d_{\ell,\lambda}\psi_\lambda$$

Finally, we obtain:

$$\mathbf{f}=\sum_{\ell,\lambda}d_{\ell,\lambda}\Psi_{\ell,\lambda}$$

with $d_{\ell,\lambda}=\langle\mathbf{f},\Psi_{\ell,\lambda}\rangle$, which corresponds to the wavelet series of $\mathbf{f}$ on the manifold generated by $\boldsymbol{\varepsilon}_\ell(\boldsymbol{\xi})$ in Fourier space.

3 Divergence-free wavelets for Craya decomposition

A construction of orthogonal wavelets with the help of the Fourier transform spanning each of the three-differential spaces: gradient, toroidal and poloidal can be found in [18, 19]. Here we reformulate this construction in a concise way.

3.1 Orthogonal Craya wavelets

Due to the characteristics of the Laplace operator, we know that compactly supported orthogonal divergence-free wavelets do not exist [21, 22]. As shown in [21], if compactly supported orthogonal divergence-free wavelets existed then the restriction to $[0,1]^n$ of harmonic functions (functions f such that $\Delta f=0$) on $\mathbb{R}^n$ would be a space of finite dimension, which is not the case.

A way to construct Craya wavelets is to define them in the gradient, toroidal or poloidal spaces in Fourier space, and then to transform them back to physical space. For this, if $\{\psi_{\varepsilon,j,\mathbf{k}}\}_{\varepsilon\in\{0,1\}^{3*},j\in\mathbb{Z},\mathbf{k}\in Z^3}$ is an orthogonal wavelet basis of $L^2(\mathbb{R}^3)$, then the wavelet bases of the gradient, the toroidal and the poloidal spaces are given by:

$$\widehat{\Psi^{\nabla}_{\varepsilon,j,\mathbf{k}}}(\boldsymbol{\xi})=\widehat{\psi_{\varepsilon,j,\mathbf{k}}}(\boldsymbol{\xi})\mathbf{e}_\nabla(\boldsymbol{\xi})\quad \widehat{\Psi^{\mathrm{T}}_{\varepsilon,j,\mathbf{k}}}(\boldsymbol{\xi})=\widehat{\psi_{\varepsilon,j,\mathbf{k}}}(\boldsymbol{\xi})\mathbf{e}_{\mathrm{T}}(\boldsymbol{\xi})\quad \widehat{\Psi^{\mathrm{P}}_{\varepsilon,j,\mathbf{k}}}(\boldsymbol{\xi})=\widehat{\psi_{\varepsilon,j,\mathbf{k}}}(\boldsymbol{\xi})\mathbf{e}_{\mathrm{P}}(\boldsymbol{\xi})\quad (3.1)$$

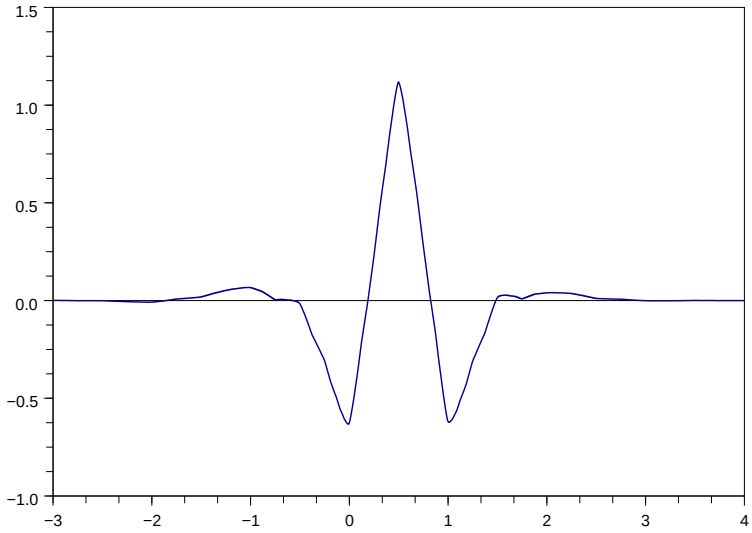

Figure 2: Coifman 12 wavelet used in the numerical experiments to construct the orthogonal Craya wavelets. Its particularity is to be quasi-symmetric.

where $\mathbf{e}_\nabla$, $\mathbf{e}_\mathrm{T}$ and $\mathbf{e}_\mathrm{P}$ are defined in (1.4).
The obtained wavelets $\Psi^\nabla_{\varepsilon,j,\mathbf{k}}$, $\Psi^\mathrm{T}_{\varepsilon,j,\mathbf{k}}$ and $\Psi^\mathrm{P}_{\varepsilon,j,\mathbf{k}}$ still remain in $\left(L^2(\mathbb{R}^3)\right)^3$, they are orthogonal, real-valued but have an infinite support. Even worse, as the functions $\boldsymbol{\xi} \mapsto \mathbf{e}_\mathrm{T}(\boldsymbol{\xi})$ and $\boldsymbol{\xi} \mapsto \mathbf{e}_\mathrm{P}(\boldsymbol{\xi})$ are discontinuous along the x_3-axis, the resulting wavelets $\Psi^\mathrm{T}_{\varepsilon,j,\mathbf{k}}$ and $\Psi^\mathrm{P}_{\varepsilon,j,\mathbf{k}}$ exhibit a slow decay at infinity (proportional to $\frac{1}{\|\boldsymbol{x}\|^2}$).

This decay problem at infinity can be circumvented by separating the vertical and horizontal scales of the wavelets. It corresponds to perform a 2D multiresolution analysis wavelet transform for the horizontal plans, and then a tensorial wavelet transform in the vertical direction:

$$\Psi_{\varepsilon,j_\mathrm{h},j_\mathrm{v},\mathbf{k}} = \eta_{\varepsilon_1,j_\mathrm{h},k_1}\eta_{\varepsilon_2,j_\mathrm{h},k_2}\psi_{j_\mathrm{v},k_3}$$

with $\eta_0 = \varphi$ and $\eta_1 = \psi$, $\varepsilon \in \{0,1\}^2 \setminus \{(0,0)\}$, $\mathbf{k} \in \mathbb{Z}^3$, and $j_\mathrm{h}, j_\mathrm{v} \in \mathbb{Z}$.

Such an operation permits us to avoid the MRA wavelet $\varphi\varphi\psi$ whose Fourier transform is non zero along the vertical axis and which interferes with the discontinuities of $\boldsymbol{\xi} \mapsto \mathbf{e}_\mathrm{T}(\boldsymbol{\xi})$ and $\boldsymbol{\xi} \mapsto \mathbf{e}_\mathrm{P}(\boldsymbol{\xi})$ along the vertical axis. At this moment the decay of the function improves from $O(\|\boldsymbol{x}\|^{-2})$ to $O(\|\boldsymbol{x}\|^{-(2+p)})$ where p is the number of zero moments of the underlying wavelet ψ. However, using this construction, the wavelets become anisotropic in the sense that they have different scales in different directions. Hence they do not constitute a multiresolution analysis anymore.

3.2 Orthogonal Craya wavelet decomposition

The orthogonal Craya wavelet decomposition of a vector field $\mathbf{u} \in \left(L^2(\mathbb{R}^3)\right)^3$ necessitates the use of the Fourier transform. It proceeds as follows:
- we first apply the Fourier transform to $\mathbf{u}$: $\mathbf{u} \mapsto \widehat{\mathbf{u}}$,

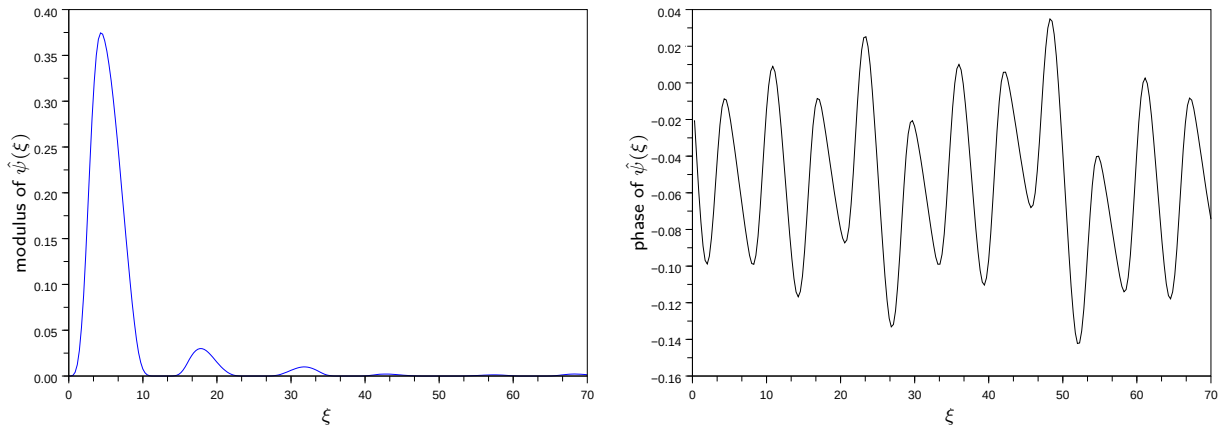

Figure 3: Fourier transform of the Coifman 12 wavelet. We represented the modulus ρ (left) and the phase θ (right) of the Fourier transform of the wavelet function: $\hat{\psi}(\xi) = \rho e^{i\theta}$ with $\rho \geq 0$ and $\theta \in [-\pi, \pi)$. We remark that ρ is mainly localized on the interval $[\pi, 2\pi]$ as usual for wavelet functions, and that θ is very close to zero due to the quasi axial symmetry of the Coifman 12 wavelet.

- then we make a change of basis in Fourier space, taking $(\mathbf{e}_\nabla, \mathbf{e}_\mathrm{T}, \mathbf{e}_\mathrm{P})$ instead of the canonical basis $(\mathbf{e}_1, \mathbf{e}_2, \mathbf{e}_3)$ (cf. Fig. 1, top):

$$\widehat{\mathbf{u}}(\boldsymbol{\xi}) = \langle \widehat{\mathbf{u}}(\boldsymbol{\xi}), \mathbf{e}_\nabla^* \rangle \mathbf{e}_\nabla + \langle \widehat{\mathbf{u}}(\boldsymbol{\xi}), \mathbf{e}_\mathrm{T}^* \rangle \mathbf{e}_\mathrm{T} + \langle \widehat{\mathbf{u}}(\boldsymbol{\xi}), \mathbf{e}_\mathrm{P}^* \rangle \mathbf{e}_\mathrm{P}$$

- then we apply the inverse Fourier transform to the three components: $\widehat{u_\nabla} = \langle \widehat{\mathbf{u}}, \mathbf{e}_\nabla^* \rangle$, $\widehat{u_\mathrm{T}} = \langle \widehat{\mathbf{u}}, \mathbf{e}_\mathrm{T}^* \rangle$ and $\widehat{u_\mathrm{P}} = \langle \widehat{\mathbf{u}}, \mathbf{e}_\mathrm{P}^* \rangle$:

$$\widehat{u_\nabla} \mapsto u_\nabla, \quad \widehat{u_\mathrm{T}} \mapsto u_\mathrm{T}, \quad \widehat{u_\mathrm{P}} \mapsto u_\mathrm{P}$$

- finally, we apply a usual wavelet decomposition to the three components u_∇, u_T and u_P. This corresponds to performing a wavelet decomposition on the manifolds $\mathbf{H}_\nabla$, $\mathbf{H}_\mathrm{T}$ and $\mathbf{H}_\mathrm{P}$, and yields the orthogonal Craya wavelet decomposition:

$$\mathbf{u} = \sum_{\varepsilon,j,\mathbf{k}} d_{\nabla\,\varepsilon,j,\mathbf{k}} \Psi_{\nabla\,\varepsilon,j,\mathbf{k}} + d_{\mathrm{T}\,\varepsilon,j,\mathbf{k}} \Psi_{\mathrm{T}\,\varepsilon,j,\mathbf{k}} + d_{\mathrm{P}\,\varepsilon,j,\mathbf{k}} \Psi_{\mathrm{P}\,\varepsilon,j,\mathbf{k}}$$

with $d_{\nabla\,\varepsilon,j,\mathbf{k}} = \langle \mathbf{u}, \Psi_{\nabla\,\varepsilon,j,\mathbf{k}} \rangle$, $d_{\mathrm{T}\,\varepsilon,j,\mathbf{k}} = \langle \mathbf{u}, \Psi_{\mathrm{T}\,\varepsilon,j,\mathbf{k}} \rangle$ and $d_{\mathrm{P}\,\varepsilon,j,\mathbf{k}} = \langle \mathbf{u}, \Psi_{\mathrm{P}\,\varepsilon,j,\mathbf{k}} \rangle$.

3.3 Biorthogonal Craya wavelets

Similarly to the definition of compactly supported divergence-free wavelets, we propose to use biorthogonal anisotropic vector-valued wavelets constructed in physical space, using derivatives. Let ψ_0, ψ_1 and ψ_2 be one-dimensional biorthogonal wavelets such that ψ_2 and ψ_1 are related with ψ_1 and ψ_0 via their derivatives $\psi_2' = 4\psi_1$ and $\psi_1' = 4\psi_0$, respectively.

We use the notation $\psi_{j,k}(x) = \psi(2^j x - k)$ and introduce the following wavelets:

$$\Psi_\nabla = \begin{bmatrix} 2^{j_1} \psi_{1,j_1,k_1} \psi_{2,j_2,k_2} \psi_{2,j_3,k_3} \\ 2^{j_2} \psi_{2,j_1,k_1} \psi_{1,j_2,k_2} \psi_{2,j_3,k_3} \\ 2^{j_3} \psi_{2,j_1,k_1} \psi_{2,j_2,k_2} \psi_{1,j_3,k_3} \end{bmatrix},$$

$$\Psi_{\mathrm{T}} = \begin{bmatrix} 2^{j_2}\psi_{2,j_1,k_1}\psi_{1,j_2,k_2}\psi_{1,j_3,k_3} \\ -2^{j_1}\psi_{1,j_1,k_1}\psi_{2,j_2,k_2}\psi_{1,j_3,k_3} \\ 0 \end{bmatrix}$$

and

$$\Psi_{\mathrm{P}} = \begin{bmatrix} 2^{j_1+j_3}\psi_{1,j_1,k_1}\psi_{2,j_2,k_2}\psi_{1,j_3,k_3} \\ 2^{j_2+j_3}\psi_{2,j_1,k_1}\psi_{1,j_2,k_2}\psi_{1,j_3,k_3} \\ -(2^{2j_1}\psi_{0,j_1,k_1}\psi_{2,j_2,k_2}\psi_{2,j_3,k_3} + 2^{2j_2}\psi_{2,j_1,k_1}\psi_{0,j_2,k_2}\psi_{2,j_3,k_3}) \end{bmatrix}.$$

The problem with Ψ_{P} is that it is not a wavelet *stricto sensus* but a vaguelette since its third component can be expressed as the 2-D Laplacian of a wavelet. This makes the decomposition in such a basis quite difficult.

On figures 5 and 6, we compare gradient, toroidal and poloidal Crayalets obtained respectively thanks to the Fourier transform (based on Coiflet 12 wavelets) and the biorthogonal ones (based on cubic spline wavelets and the formulae above) using in both cases the anisotropic construction. The Coiflet 12 wavelet has the advantage of being relatively smooth ($C^{1.707}$), and nearly symmetric. That is why it is often used in fluid dynamics analysis, see e.g. [13]. Cubic spline wavelets, on their side, are C^2, symmetric and easy to implement. Shown are isosurfaces of the norm of the vector-valued wavelets, i.e. $\|\boldsymbol{\Psi}(\boldsymbol{x})\| = Const.$

We observe that both families (orthogonal and biorthogonal) look similar. We also observe that the gradient Crayalets form a six-branches 'squeaker bone', that toroidal Crayalets look like 'pebbles' and poloidal Crayalets like 'amphora with handles'. This corresponds to the kind of vector fields we encounter in each case (see fig. 1 bottom, right).

3.4 The biorthogonal Craya wavelet transform

In the following we explain how to obtain a biorthogonal Crayalet transform. Suppose we start from a divergence-free vector-valued function $\mathbf{u} \in \left(L^2(\mathcal{T}^3)\right)^3$ with $\mathcal{T} = \mathbb{R}/\mathbb{Z}$. If it is not divergence-free, we can apply the wavelet Helmholtz decomposition [11]. First we apply a wavelet 2-dimensional Helmholtz decomposition (see [11]) on u_1 and u_2 excluding the x_3-direction from the decomposition:

$$\begin{bmatrix} u_1(\mathbf{x}) \\ u_2(\mathbf{x}) \end{bmatrix} = \sum_{\mathbf{j}\in\mathbb{Z}^2,\mathbf{k}\in\mathbb{Z}^2} d_{\mathbf{jk}}^{\mathrm{T2D}}(x_3) \begin{bmatrix} 2^{j_2}\psi_{2,j_1,k_1}(x_1)\psi_{1,j_2,k_2}(x_2) \\ -2^{j_1}\psi_{1,j_1,k_1}(x_1)\psi_{2,j_2,k_2}(x_2) \end{bmatrix} + d_{\mathbf{jk}}^{\tilde{\nabla}\mathrm{2D}}(x_3) \begin{bmatrix} 2^{j_1}\psi_{1,j_1,k_1}(x_1)\psi_{2,j_2,k_2}(x_2) \\ 2^{j_2}\psi_{2,j_1,k_1}(x_1)\psi_{1,j_2,k_2}(x_2) \end{bmatrix}$$

Then we make 1-dimensional wavelet transforms of $x_3 \mapsto d_{\mathbf{jk}}^{\mathrm{T2D}}(x_3)$ and $d_{\mathbf{jk}}^{\tilde{\nabla}\mathrm{2D}}(x_3)$ yielding:

$$\begin{bmatrix} u_1(\mathbf{x}) \\ u_2(\mathbf{x}) \\ 0 \end{bmatrix} = \sum_{\mathbf{j}\in\mathbb{Z}^3,\mathbf{k}\in\mathbb{Z}^3} d_{\mathbf{jk}}^{\mathrm{T}}\Psi_{\mathrm{T}\mathbf{jk}} + d_{\mathbf{jk}}^{\nabla\mathrm{2D}} \begin{bmatrix} 2^{j_1}\psi_{1,j_1,k_1}(x_1)\psi_{2,j_2,k_2}(x_2)\psi_{1,j_3,k_3}(x_3) \\ 2^{j_2}\psi_{2,j_1,k_1}(x_1)\psi_{1,j_2,k_2}(x_2)\psi_{1,j_3,k_3}(x_3) \\ 0 \end{bmatrix}$$

Thereafter we decompose u_3 into the 2-dimensional horizontal vaguelette basis $\frac{1}{16}\Delta\psi_2\psi_2 = 2^{2j_1}\psi_0\psi_2 + 2^{2j_2}\psi_2\psi_0$:

$$u_3(\mathbf{x}) = \sum_{\mathbf{j}\in\mathbb{Z}^2,\mathbf{k}\in\mathbb{Z}^2} d_{\mathbf{jk}}^{\tilde{\mathrm{P}}\,3}(x_3)\left(2^{2j_1}\psi_{0,j_1,k_1}(x_1)\psi_{2,j_2,k_2}(x_2) + 2^{2j_2}\psi_{2,j_1,k_1}(x_1)\psi_{0,j_2,k_2}(x_2)\right)$$

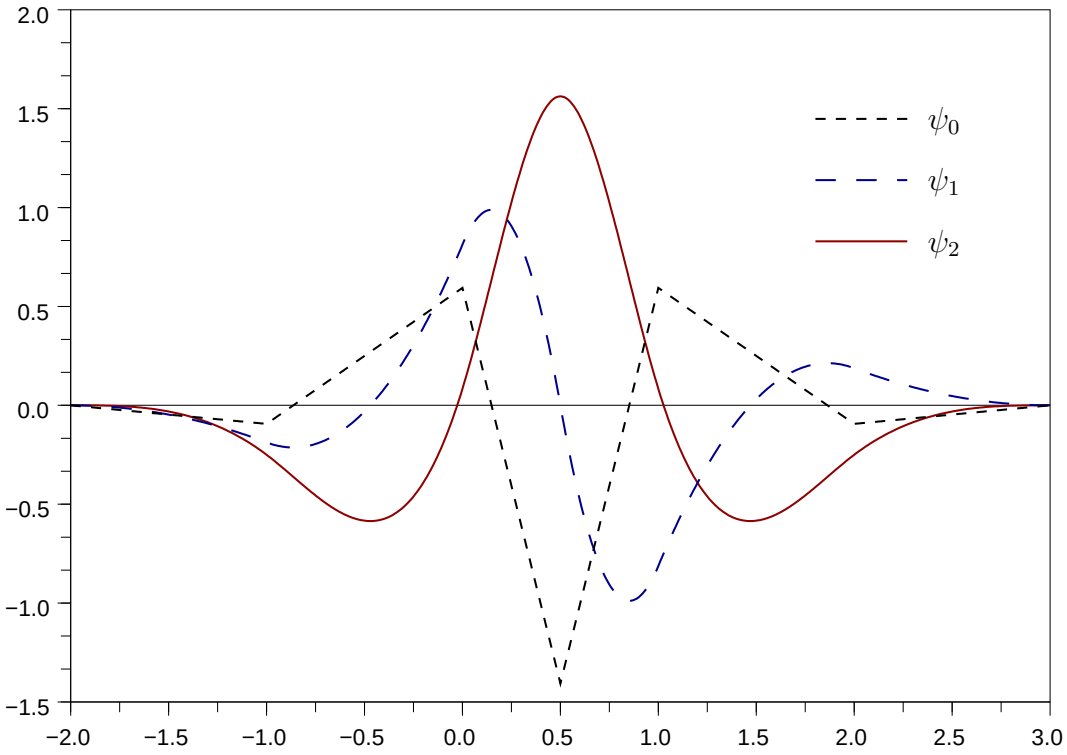

Figure 4: Linear spline wavelets ψ_0 (dotted line), quadratic spline wavelet ψ_1 (dashed line) and cubic spline wavelet ψ_2 (solid line) used for biorthogonal wavelets in the numerical experiments, $\psi_2' = 4\,\psi_1$ and $\psi_1' = 4\,\psi_0$.

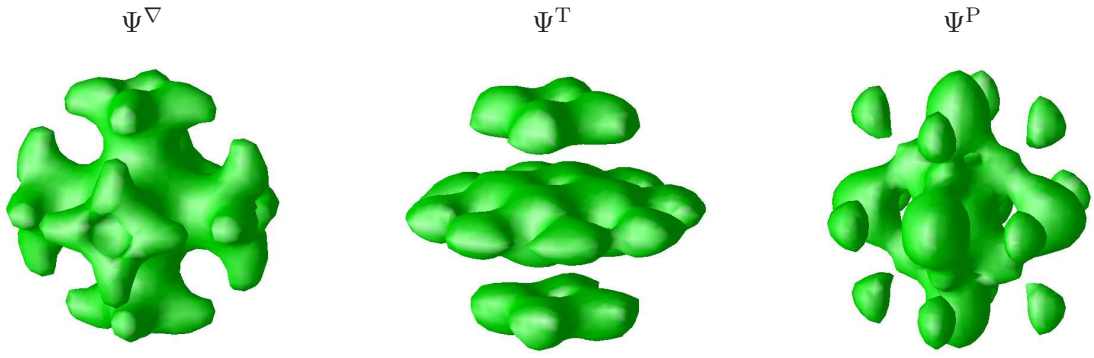

Figure 5: Orthogonal gradient (left), toroidal (middle) and poloidal (right) anisotropic wavelets built with the Fourier transform. Isosurface value $= 4/9 \times \max(|\Psi_{\nabla}|)$ for gradient wavelet, $= \max(|\Psi^{\mathrm{T}}|)/3$ for toroidal wavelet and $= 5/24 \times \max(|\Psi_{\mathrm{P}}|)$ for poloidal wavelet. Note that $\max(|\Psi^{\nabla}|) = 0.75\ \max(|\Psi^{\mathrm{T}}|)$ and $\max(|\Psi^{\mathrm{P}}|) = 1.6\ \max(|\Psi^{\mathrm{T}}|)$, although these three wavelets have the same L^2-norm.

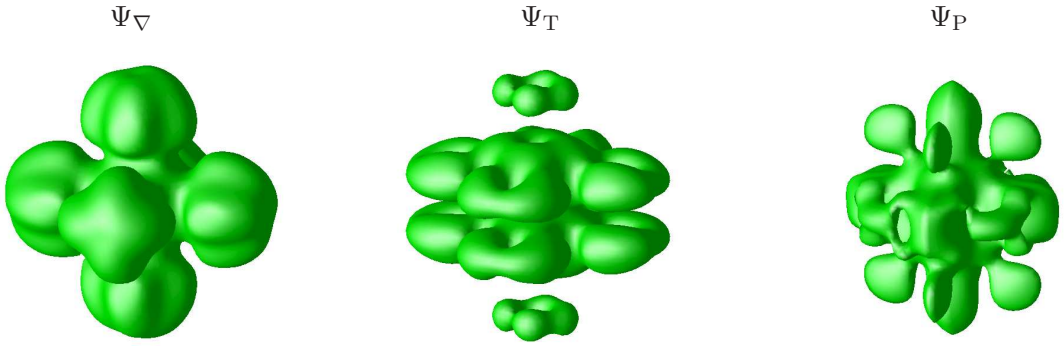

Figure 6: Biorthogonal gradient (left), toroidal (middle) and poloidal (right) anisotropic wavelets built from spline wavelets of figure 4 at scale $j_1 = j_2 = j_3 = 3$. Isosurface value $= \max(|\Psi_\nabla|)/6$ for gradient wavelet, $= \max(|\Psi_T|)/6$ for toroidal wavelet and $= \max(|\Psi_P|)/14$ for poloidal wavelet. The three wavelets do not have the same L^2-norm.

and apply a classical wavelet transform along the third direction:

$$u_3(\mathbf{x}) = \sum_{\mathbf{j}\in\mathbb{Z}^3,\mathbf{k}\in\mathbb{Z}^3} d^{\mathrm{P}\,3}_{\mathbf{jk}} \left(2^{2j_1}\psi_{0,j_1,k_1}(x_1)\psi_{2,j_2,k_2}(x_2) + 2^{2j_2}\psi_{2,j_1,k_1}(x_1)\psi_{0,j_2,k_2}(x_2)\right)\psi_{2,j_3,k_3}(x_3)$$

Then we obtain the poloidal wavelet coefficient by solving a square minimization and putting:

$$d^{\mathrm{P}}_{\mathbf{jk}} = \frac{2^{j_3} d^{\nabla 2\mathrm{D}}_{\mathbf{jk}} - (2^{2j_1} + 2^{2j_2}) d^{\mathrm{P}\,3}_{\mathbf{jk}}}{2^{2j_1} + 2^{2j_2} + 2^{2j_3}}.$$

Therefore we obtain:

$$\mathbf{u} = \sum_{\mathbf{j}\in\mathbb{Z}^3,\mathbf{k}\in\mathbb{Z}^3} d^{\mathrm{T}}_{\mathbf{jk}}\Psi_{\mathrm{T}\mathbf{jk}} + d^{\mathrm{P}}_{\mathbf{jk}}\Psi_{\mathrm{P}\mathbf{jk}}. \tag{3.2}$$

3.5 Quasi-Craya divergence-free wavelets

As we said in section 3.3, exact biorthogonal Crayalets are difficult to apply because of the mathematical expression the poloidal Crayalet takes. In this section, we will present approximate Crayalets which can be applied through a straightforward fast wavelet transform. Instead of formulas of section 3.3, we propose to use linear combinations of:

$$\Psi_{\mathrm{div},1} = \begin{bmatrix} 0 \\ 2^{j_3}\psi_{0,j_1,k_1}\psi_{1,j_2,k_2}\psi_{0,j_3,k_3} \\ -2^{j_2}\psi_{0,j_1,k_1}\psi_{0,j_2,k_2}\psi_{1,j_3,k_3} \end{bmatrix},\ \Psi_{\mathrm{div},2} = \begin{bmatrix} -2^{j_3}\psi_{1,j_1,k_1}\psi_{0,j_2,k_2}\psi_{0,j_3,k_3} \\ 0 \\ 2^{j_1}\psi_{0,j_1,k_1}\psi_{0,j_2,k_2}\psi_{1,j_3,k_3} \end{bmatrix}$$

and

$$\Psi_{\mathrm{div},3} = \begin{bmatrix} 2^{j_2}\psi_{1,j_1,k_1}\psi_{0,j_2,k_2}\psi_{0,j_3,k_3} \\ -2^{j_1}\psi_{0,j_1,k_1}\psi_{1,j_2,k_2}\psi_{0,j_3,k_3} \\ 0 \end{bmatrix}$$

from [9].
We take $\Psi_T = \Psi_{\mathrm{div},3}$ as we did in section 3.3, and we combine the two other wavelets which have a vertical component ($\mathbf{e}_3$):

$$\Psi_{\mathrm{qP}} = -2^{j_1}\Psi_{\mathrm{div},2} + 2^{j_2}\Psi_{\mathrm{div},1}$$

where the letters 'qP' stands for quasi-poloidal. Hence we need only two different 1D wavelets ψ_0 and ψ_1 linked by differentiation: $\psi_1' = 4\psi_0$ instead of three. We can remark that the wavelets $\Psi_{\mathrm{div},3,\mathbf{j},\mathbf{k}}$ and $\Psi_{\mathrm{qP},\mathbf{j},\mathbf{k}}$ are orthogonal for any given scale $\mathbf{j}$ and location $\mathbf{k}$.

Following [11], the decomposition in the quasi-Craya divergence-free wavelet basis derives from the usual divergence-free wavelet decomposition:

$$\mathbf{u}(\mathbf{x}) = \left| \begin{array}{l} u_1(\mathbf{x}) = \sum_{\mathbf{j},\mathbf{k}\in\mathbb{Z}^3} d_{1\,\mathbf{j},\mathbf{k}}\ \psi_1(2^{j_1}x_1 - k_1)\psi_0(2^{j_2}x_2 - k_2)\psi_0(2^{j_3}x_3 - k_3) \\ u_2(\mathbf{x}) = \sum_{\mathbf{j},\mathbf{k}\in\mathbb{Z}^3} d_{2\,\mathbf{j},\mathbf{k}}\ \psi_0(2^{j_1}x_1 - k_1)\psi_1(2^{j_2}x_2 - k_2)\psi_0(2^{j_3}x_3 - k_3) \\ u_3(\mathbf{x}) = \sum_{\mathbf{j},\mathbf{k}\in\mathbb{Z}^3} d_{3\,\mathbf{j},\mathbf{k}}\ \psi_0(2^{j_1}x_1 - k_1)\psi_0(2^{j_2}x_2 - k_2)\psi_1(2^{j_3}x_3 - k_3) \end{array} \right.$$

Then the toroidal and quasi-poloidal wavelet coefficients of $\mathbf{u}$ are given by:

$$\mathbf{u} = \sum_{\mathbf{j}\in\mathbb{Z}^n}\sum_{\mathbf{k}\in\mathbb{Z}^n} d_{\mathrm{T}\,\mathbf{j},\mathbf{k}}\ \Psi_{\mathrm{T}\,\mathbf{j},\mathbf{k}} + \sum_{\mathbf{j}\in\mathbb{Z}^n}\sum_{\mathbf{k}\in\mathbb{Z}^n} d_{\mathrm{qP}\,\mathbf{j},\mathbf{k}}\ \Psi_{\mathrm{qP}\,\mathbf{j},\mathbf{k}} + \sum_{\mathbf{j}\in\mathbb{Z}^n}\sum_{\mathbf{k}\in\mathbb{Z}^n} d_{\mathrm{N}\,\mathbf{j},\mathbf{k}}\ \Psi_{\mathrm{N}\,\mathbf{j},\mathbf{k}} \tag{3.3}$$

where the wavelet $\Psi_{\mathrm{N}\,\mathbf{j},\mathbf{k}}$ span the remaining space. It can be viewed as an approximate gradient function:

$$\Psi_{\mathrm{N}} = \left[\begin{array}{c} 2^{j_1}\psi_{1,j_1,k_1}\psi_{0,j_2,k_2}\psi_{0,j_3,k_3} \\ 2^{j_2}\psi_{0,j_1,k_1}\psi_{1,j_2,k_2}\psi_{0,j_3,k_3} \\ 2^{j_3}\psi_{0,j_1,k_1}\psi_{0,j_2,k_2}\psi_{1,j_3,k_3} \end{array} \right]$$

The wavelet coefficients $d_{\mathrm{T}\,\mathbf{j},\mathbf{k}}$, $d_{\mathrm{qP}\,\mathbf{j},\mathbf{k}}$ and $d_{\mathrm{N}\,\mathbf{j},\mathbf{k}}$ are solutions of the linear system

$$\left[\begin{array}{ccc} \omega_2 & \omega_1\omega_3 & \omega_1 \\ -\omega_1 & \omega_2\omega_3 & \omega_2 \\ 0 & -(\omega_1^2+\omega_2^2) & \omega_3 \end{array} \right] \left[\begin{array}{c} d^{\mathrm{div}}_{\mathrm{T}\,\mathbf{j},\mathbf{k}} \\ d^{\mathrm{div}}_{\mathrm{qP}\,\mathbf{j},\mathbf{k}} \\ d_{\mathrm{N}\,\mathbf{j},\mathbf{k}} \end{array} \right] = \left[\begin{array}{c} d_{1\,\mathbf{j},\mathbf{k}} \\ d_{2\,\mathbf{j},\mathbf{k}} \\ d_{3\,\mathbf{j},\mathbf{k}} \end{array} \right] \tag{3.4}$$

We thus obtain:

$$\left[\begin{array}{c} d^{\mathrm{div}}_{\mathrm{T}\,\mathbf{j},\mathbf{k}} \\ d^{\mathrm{div}}_{\mathrm{qP}\,\mathbf{j},\mathbf{k}} \\ d_{\mathrm{N}\,\mathbf{j},\mathbf{k}} \end{array} \right] = \frac{1}{|\boldsymbol{\omega}|^2|\boldsymbol{\omega}_h|^2} \left[\begin{array}{ccc} |\boldsymbol{\omega}|^2\omega_2 & -|\boldsymbol{\omega}|^2\omega_1 & 0 \\ \omega_1\omega_3 & \omega_2\omega_3 & -|\boldsymbol{\omega}_h|^2 \\ |\boldsymbol{\omega}_h|^2\omega_1 & |\boldsymbol{\omega}_h|^2\omega_2 & |\boldsymbol{\omega}_h|^2\omega_3 \end{array} \right] \left[\begin{array}{c} d_{1\,\mathbf{j},\mathbf{k}} \\ d_{2\,\mathbf{j},\mathbf{k}} \\ d_{3\,\mathbf{j},\mathbf{k}} \end{array} \right] \tag{3.5}$$

where $|\boldsymbol{\omega}|^2 = \omega_1^2 + \omega_2^2 + \omega_3^2$ and $|\boldsymbol{\omega}_h|^2 = \omega_1^2 + \omega_2^2$.
Therefore, we have constructed a divergence-free wavelet basis which has the properties of a Riesz basis, and almost discriminates the toroidal part from the poloidal part.

3.6 MRA biorthogonal Craya wavelets

The toroidal and poloidal wavelet bases are generated by seven different wavelets deriving from the $L^2(\mathbb{R}^3)$ basis $(\eta^{\varepsilon_1}\times\eta^{\varepsilon_2}\times\eta^{\varepsilon_3})_{\boldsymbol{\varepsilon}\in\{0,1\}^3\setminus\{(0,0,0)\}}$, with $\eta^0 = \varphi$ and $\eta^1 = \psi$. The first difficulty comes from the construction of a well conditioned fast transform algorithm. For instance, the toroidal wavelets for $\varepsilon = (0,0,1)$ should be:

$$\Psi_{\mathrm{T}}^{(0,0,1)} = \left(\begin{array}{c} \partial_{x_2} \\ -\partial_{x_1} \\ 0 \end{array} \right) \varphi_1\varphi_1\psi_0 = \left| \begin{array}{l} \varphi_1(\varphi_0 - \varphi_0(\cdot-1))\psi_0 \\ -(\varphi_0 - \varphi_0(\cdot-1))\varphi_1\psi_0 \\ 0 \end{array} \right.$$

Hence we still have the compact support property, but this is no longer a wavelet, in particular the dual wavelet is not compactly supported. This excludes any straightforward vector-valued wavelet decomposition using a MRA construction.

3.7 Generalization to higher dimensions

The Craya decomposition can be generalized to a number of dimensions higher than three, distinguishing a preferential two-dimensional divergence-free vector space, then a three-dimensional divergence-free vector space containing the previous one, etc... until we obtain the whole divergence-free space on $\mathbb{R}^n$. The unit vectors, defined in Fourier space are given by:

$$\mathbf{e}_{\mathrm{T}} = \frac{1}{\sqrt{\xi_1^2+\xi_2^2}} \begin{bmatrix} i\xi_2 \\ -i\xi_1 \\ 0 \\ \vdots \\ 0 \end{bmatrix} \qquad \mathbf{e}_{\mathrm{P},1} = \frac{1}{\sqrt{\xi_1^2+\xi_2^2+\xi_3^2}\sqrt{\xi_1^2+\xi_2^2}} \begin{bmatrix} \xi_3\xi_1 \\ \xi_3\xi_2 \\ -(\xi_1^2+\xi_2^2) \\ 0 \\ \vdots \\ 0 \end{bmatrix}$$

and generally for $1 \leq m \leq n-2$

$$\mathbf{e}_{\mathrm{P},m} = \frac{1}{\sqrt{\sum_{k=1}^{m+2}\xi_k^2}\sqrt{\sum_{k=1}^{m+1}\xi_k^2}} \begin{bmatrix} \xi_{m+2}\xi_1 \\ \vdots \\ \xi_{m+2}\xi_{m+1} \\ -(\sum_{k=1}^{m+1}\xi_k^2) \\ 0 \\ \vdots \\ 0 \end{bmatrix}$$

In the orthogonal case (sec. 3.1) and the biorthogonal case (sec. 3.3) Crayalet bases, similar to those in three dimensions, can be used. We can construct quasi-Crayalets similarly as we did in three dimensions in section 3.5. Using the tensorial wavelets in $(W_{j_1}^1 \otimes W_{j_2}^0 \otimes \cdots \otimes W_{j_n}^0) \times \cdots \times (W_{j_1}^0 \otimes \cdots \otimes W_{j_{n-1}}^0 \otimes W_{j_n}^1)$, with $W_j^1 = span\{\psi_{1\,j,k}\}_{k\in\mathbb{Z}}$, $W_j^0 = span\{\psi_{0\,j,k}\}_{k\in\mathbb{Z}}$ and $\psi_1' = 4\psi_0'$, we just replace the matrix in (3.4) by

$$A = \begin{bmatrix} \omega_2 & \omega_3\omega_1 & \dots & \omega_m\omega_1 & \dots & \omega_n\omega_1 & \omega_1 \\ -\omega_1 & \omega_3\omega_2 & \dots & \vdots & \dots & \omega_n\omega_2 & \omega_2 \\ 0 & -(\omega_1^2+\omega_2^2) & \ddots & \vdots & \dots & \vdots & \vdots \\ \vdots & 0 & \ddots & \omega_m\omega_{m-1} & \dots & \vdots & \vdots \\ \vdots & \vdots & \ddots & -\sum_{k=1}^{m-1}\omega_k^2 & \ddots & \vdots & \vdots \\ \vdots & \vdots & \ddots & 0 & \ddots & \vdots & \vdots \\ \vdots & \vdots & \dots & \vdots & \ddots & \omega_n\omega_{n-1} & \vdots \\ 0 & 0 & \dots & 0 & \dots & -\sum_{k=1}^{n-1}\omega_k^2 & \omega_n \end{bmatrix} \tag{3.6}$$

We obtain a divergence-free wavelet Riesz basis which approximately performs the Craya decomposition, in the sense that as the basis functions are not perfect Crayalets, the gradient, the toroidal and each of the $n-2$ poloidal wavelet spaces concentrate most of the corresponding gradient, toroidal and poloidal flow energy respectively.

Notice that it is the only divergence-free wavelet transform for which the orthogonal matrix $A = (a_{ij})$ is zero for $i \geq j+2$. This can be shown by recurrence: in 2D, there is only one unitary divergence-free vector, $(\omega_2/|\boldsymbol{\omega}|, -\omega_1/|\boldsymbol{\omega}|)$. Let us assume that we have

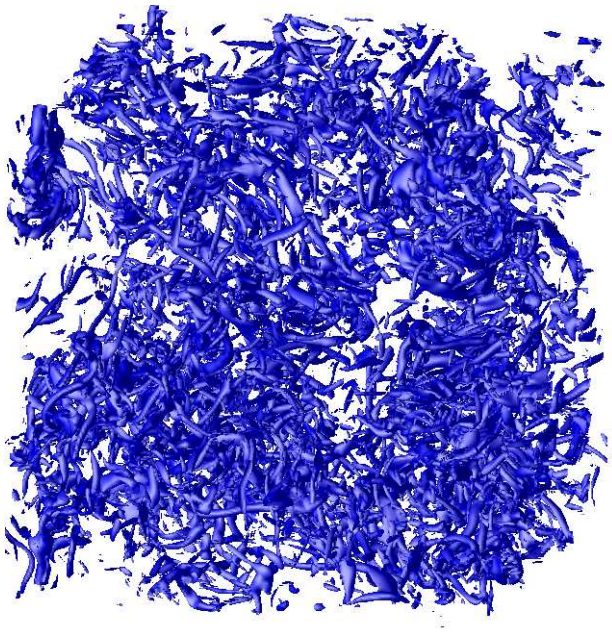

Figure 7: Isosurface of vorticity of an isotropic turbulent flow from [33]. Here we plotted the iso-value $= 0.156 \max(|\boldsymbol{\omega}(\mathbf{x})|)$.

$m-2$ orthonormal vectors $(\mathbf{e}_1, \ldots, \mathbf{e}_{m-2})$, orthogonal to $\boldsymbol{\omega}$, then there exists only one vector $\pm\mathbf{e}_{m-1}$ of size m such that $(\boldsymbol{\omega}/|\boldsymbol{\omega}|, \mathbf{e}_1, \ldots, \mathbf{e}_{m-1})$ forms an orthonormal basis of $\mathbb{R}^m$.

4 Numerical experiments

In this section, we test the Craya wavelets to analyze different turbulent flows computed by direct numerical simulation. In section 4.1, we visualize the result of the classical Craya decomposition of an isotropic turbulent flow. In section 4.2, we compress a vorticity field of isotropic turbulence with biorthogonal spline Craya wavelets from section 3.3. In section 4.3, we compare the performance of orthogonal Craya wavelets (from section 3.1) with various anisotropies applied to three different types of turbulence: isotropic, rotating and stratified flows. In this section, we used velocity fields for the decomposition.

4.1 Visualization of the Craya decomposition

We present the result of a Craya decomposition made through Fourier transform of an isotropic turbulent flow field (Fig. 7), in Fig. 8. This field has been computed by DNS at resolution 256^3 and Taylor micro-scale Reynolds number of $Re_\lambda = 140$ [33]. The Craya decomposition splits the total field into two fields with almost equal enstrophy: $\|\boldsymbol{\omega}_{\rm tot}\|^2_{L^2} = \|\boldsymbol{\omega}_{\rm T}\|^2_{L^2} + \|\boldsymbol{\omega}_{\rm P}\|^2_{L^2}$. The Craya decomposition using biorthogonal spline wavelets and algorithms presented in section 3.2 and reference [11] was tested and provided almost the same results, the only difference coming from the spline approximation.

When making a classical Craya decomposition of the field shown in Fig. 7, we observe that the entangled vortex tubes in Fig. 7 are split into horizontal (Fig. 8, left) and vertical contributions (Fig. 8, right). Both have about the same intensity, which reflects the fact

Toroidal vorticity

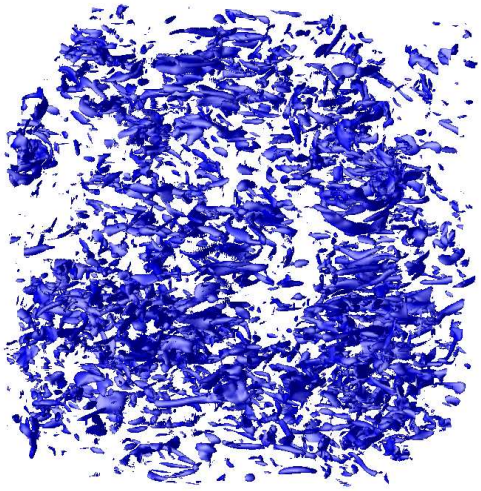

Poloidal vorticity

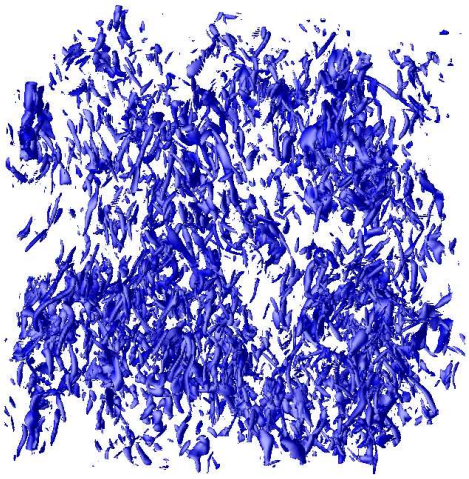

Figure 8: Isosurface of vorticity of the toroidal part of the flow (left), and poloidal part (right) obtained from the Fourier transform. For both we use the iso-value = 0.135 $\max(|\boldsymbol{\omega}_{\mathrm{tot}}(\mathbf{x})|)$.

that the flow is isotropic.

4.2 Compression of a vorticity field of isotropic turbulence with biorthogonal Craya wavelets

With biorthogonal Crayalets derived from cubic spline wavelets and its derivatives (see Fig. 6), we compressed the turbulent field shown in Fig. 7.

In Fig. 9, we present the relative error $\frac{\|\tilde{\boldsymbol{\omega}}-\boldsymbol{\omega}\|_{L^2}}{\|\boldsymbol{\omega}\|_{L^2}}$ after thresholding the expansion (3.2) with different L^2-thresholds. Here $\tilde{\boldsymbol{\omega}}$ stands for the non-linear wavelet approximation of $\boldsymbol{\omega}$. Due to the better conditioning of the toroidal wavelet basis, the toroidal part of the flows has a better compression rate than the poloidal part. The error on the total field behaves as an average between its two components, toroidal and poloidal. The limit on the error in Fig. 9 comes from the spline approximation we need in order to use biorthogonal spline wavelets. If we do not use any approximation (Fig. 10), the L^2-error goes to zero.

As shown in [10], the biorthogonal anisotropic wavelets do not perform well for compression. When the first coefficients are added, the L^2-error begins to increase instead of decreasing. As a result, we do not make any direct comparison with orthogonal Crayalets. Regarding compression issues, the anisotropic biorthogonal wavelets are not useful and shall be discarded (see also [10]).

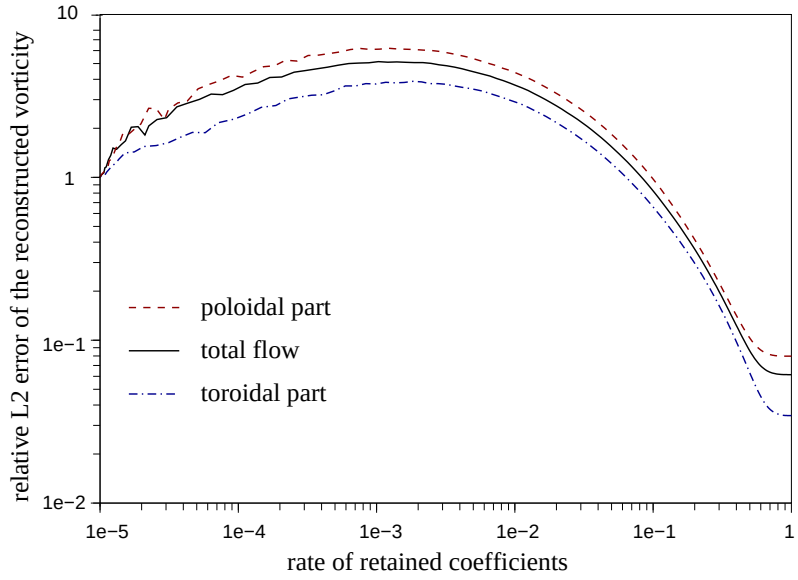

Figure 9: Compression (in logarithmic scale) obtained with anisotropic biorthogonal spline Craya wavelets (toroidal+poloidal) for isotropic turbulence vorticity.

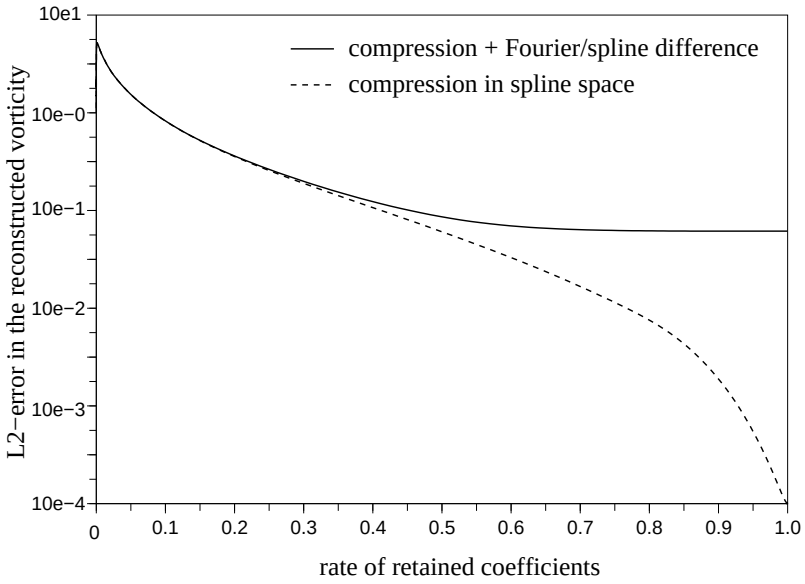

Figure 10: Compressions with and without projection on the spline space for isotropic turbulence vorticity.

4.3 Orthogonal Craya wavelet analysis of turbulent fields

We analyze three types of turbulent fields: isotropic, rotating and stratified flow. The data computed by DNS using classical Fourier methods comes from Liechtenstein et al. [24].

In this experiment, we use orthogonal Craya wavelets based on Coifman-12 filter with different scale properties:

- the anisotropic wavelets with only one wavelet function and three scale parameters: $\Psi_{(j_1,j_2,j_3),\mathbf{k}}(\boldsymbol{x}) = \psi_{j_1k_1}(x_1)\psi_{j_2k_2}(x_2)\psi_{j_3k_3}(x_3)$. Following the construction of section 3.1, the resulting orthogonal Crayalets are represented in Fig. 13.

- The isotropic wavelets with seven wavelet functions and one scale parameter: $\Psi_{\varepsilon,j,\mathbf{k}}(\boldsymbol{x}) = \eta^{\varepsilon_1}_{j_1k_1}(x_1)\eta^{\varepsilon_2}_{j_2k_2}(x_2)\eta^{\varepsilon_3}_{j_3k_3}(x_3)$, with $\varepsilon \in \{0,1\}^3 \setminus \{(0,0,0)\}$, and the convention $\eta^0 = \varphi$ and $\eta^1 = \psi$. These are represented in Fig. 14.

- Wavelets with a decorrelation between the vertical and the horizontal scales. This construction necessitates three different wavelet functions and two scale parameters: $\Psi_{\varepsilon,(j_\mathrm{h},j_\mathrm{v}),\mathbf{k}}(\boldsymbol{x}) = \eta^{\varepsilon_1}_{j_\mathrm{h}k_1}(x_1)\eta^{\varepsilon_2}_{j_\mathrm{h}k_2}(x_2)\psi_{j_\mathrm{v}k_3}(x_3)$, with $\varepsilon \in \{0,1\}^2 \setminus \{(0,0)\}$. The motivation for constructing these wavelets is provided in the last paragraph of section 3.1. The resulting Crayalets are visualized in Fig. 15.

We apply these orthogonal Craya wavelet decompositions to the velocity fields of three different turbulent flows: a statistically isotropic flow, a rotating flow and a stratified flow.

The poloidal and the toroidal parts of the flows behave similarly for the three cases as if we use isotropic wavelets, which is illustrated by the compression curves shown in Fig. 16. However when we switch to anisotropic wavelets (and h/v decorrelated wavelets), stratified flow yields a much better compression of the toroidal part, whereas the rotating flow shows a slightly better compression of the poloidal part as reflected by the results given in Fig. 17.

One observation is that stratified flow compresses better with anisotropic wavelets than with isotropic ones. For the other flow fields, the three wavelets (isotropic, anisotropic and horizontal/vertical decorrelated wavelets) yield similar compression rates as shown in Fig. 18.

When we compare the three flows in Fig. 19 in terms of the rate of retained wavelet coefficients, we observe that we get with Craya wavelets the best compression for stratified flows followed by rotating flows and then isotropic turbulence. This result is more pronounced for anisotropic wavelets (Fig. 19, right) than for isotropic wavelets (Fig. 19, left).

5 Conclusion

The construction of vector-valued functional bases satisfying additional constraints, e.g. incompressibility, provides new instruments for mathematical analysis of partial differential equations arising in fluid mechanics, in particular the Euler and Navier-Stokes equations, and for their numerical discretization and simulation. In the present paper we proposed a new construction of compactly supported Crayalets using biorthogonal wavelet bases. Therewith three-dimensional divergence-free vector fields can be decomposed efficiently into horizontal and vertical contributions, in a spirit similar to the Fourier-based

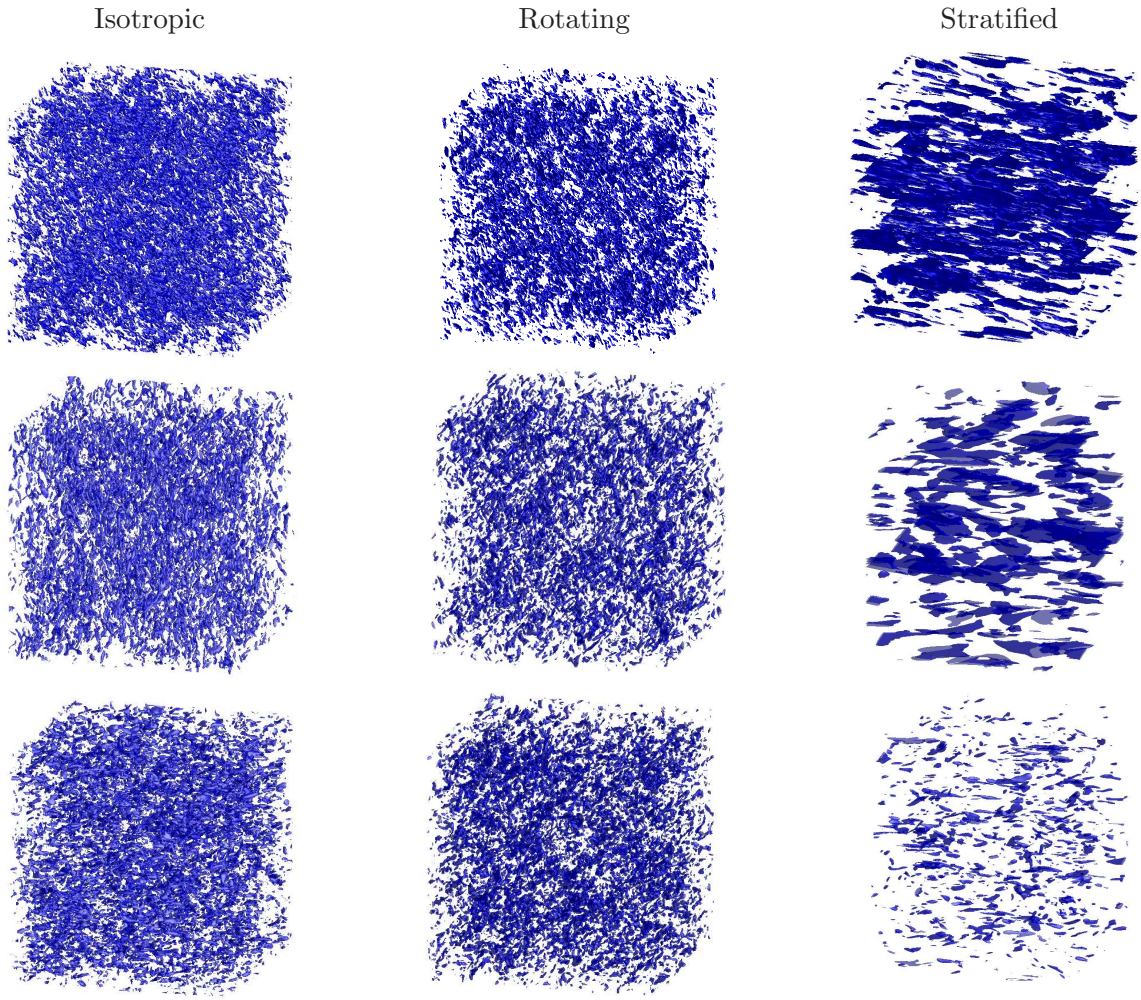

Figure 11: Isosurface of vorticity of isotropic turbulence (left), rotating turbulence (middle) and stratified turbulence (right), with total field (top), curl of the toroidal part (middle), and curl of the poloidal part (bottom). Sub-sampled cubes of 256^3 from a 512^3 direct numerical simulation [24]. Isotropic: iso-value $\omega_0 = 0.324\ \max(|\boldsymbol{\omega}_{\rm tot}(\mathbf{x})|)$ enstrophy $E = 2.83$, rotating: $\omega_0 = 0.324\ \max(|\boldsymbol{\omega}_{\rm tot}(\mathbf{x})|)$, $E = 3.68$ and stratified: $\omega_0 = 0.429\ \max(|\boldsymbol{\omega}_{\rm tot}(\mathbf{x})|)$, $E = 4.53$.

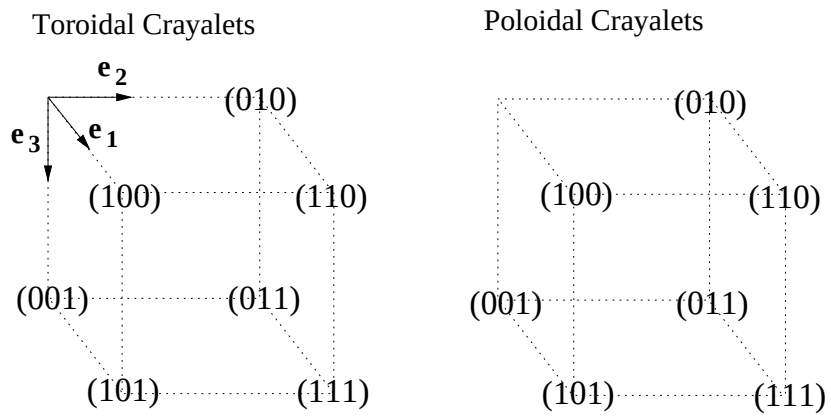

Figure 12: Arrangement of the Crayalets adopted in the following representations. The 0 indicates a low frequency function in this direction, i.e. φ in the isotropic case and $\psi(\frac{\cdot}{2})$ in the anisotropic case, while 1 indicates a high frequency function, i.e. ψ. As we have three different directions and exclude the (000) case which is not a wavelet, there are 7 toroidal wavelets and 7 poloidal wavelets.

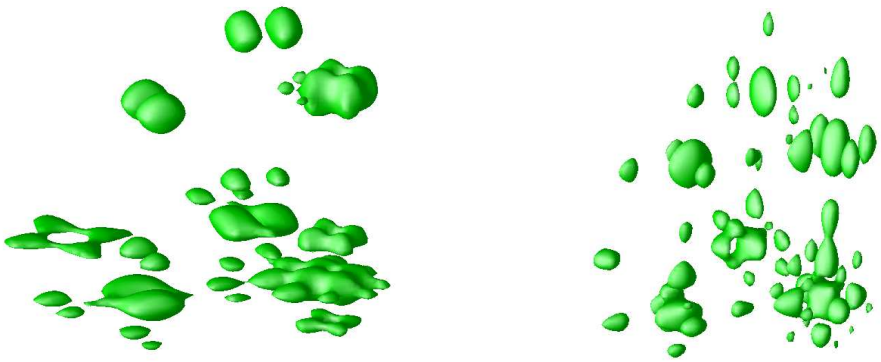

Figure 13: Toroidal (left) and poloidal (right) anisotropic orthogonal wavelets. Isosurface ($\|\Psi\|^2 = 1.5 \cdot 10^{-4}$ with $\max(\|\Psi\|^2) = 23.2 \cdot 10^{-4}$) of the modulus of the div-free vector-valued wavelets in $\mathbb{R}^3$. The wavelets are normalized in L^2 and arranged according to Fig. 12.

Craya-Herring decomposition. The latter has been applied to different kinds of homogeneous flows encountered in geophysical fluid dynamics. Compared to previous constructions of orthogonal Crayalets [18], which are based on the Fourier transform, the Crayalet basis functions proposed here are compactly supported in physical space. However, orthogonality of the basis functions is not possible anymore and has to be replaced by biorthogonality. Nevertheless, this construction does not allow to provide a MRA with Crayalets.

The application of Crayalets to DNS data of different types of turbulent flows, i.e. isotropic, rotating and stratified flows, has shown that the anisotropic Crayalet construction performs better for non isotropic turbulence in terms of the compression of energy with respect to the number of retained modes than the isotropic one. For isotropic turbulence no significant difference between isotropic and anisotropic Crayalets is observed and

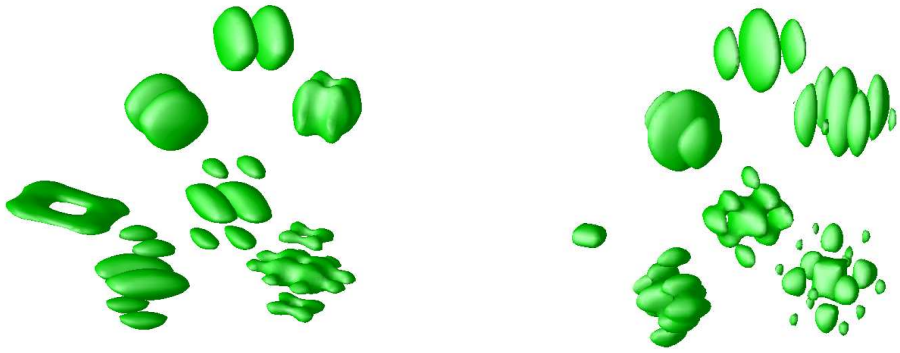

Figure 14: Toroidal (left) and poloidal (right) isotropic orthogonal wavelets. Isosurface ($\|\Psi\|^2 = 1.4 \cdot 10^{-4}$ knowing that $\max(\|\Psi\|^2) = 22.9 \cdot 10^{-4}$) of the modulus of the 14 div-free vector-valued wavelets in $\mathbb{R}^3$ (Coiflet-12) normalized in L^2.

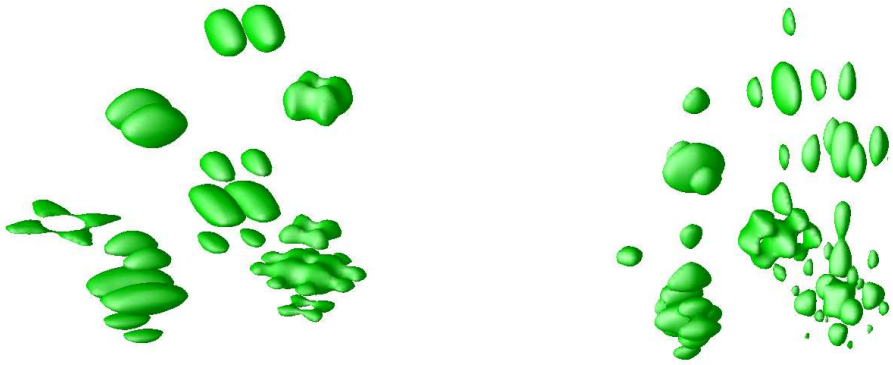

Figure 15: Toroidal (left) and poloidal (right) orthogonal wavelets with horizontal/vertical decorrelation. Isosurface ($\|\Psi\|^2 = 1.5 \cdot 10^{-4}$ with $\max(\|\Psi\|^2) = 22.4 \cdot 10^{-4}$) of the modulus of the 3 div-free vector-valued wavelets in $\mathbb{R}^3$, normalized in L^2.

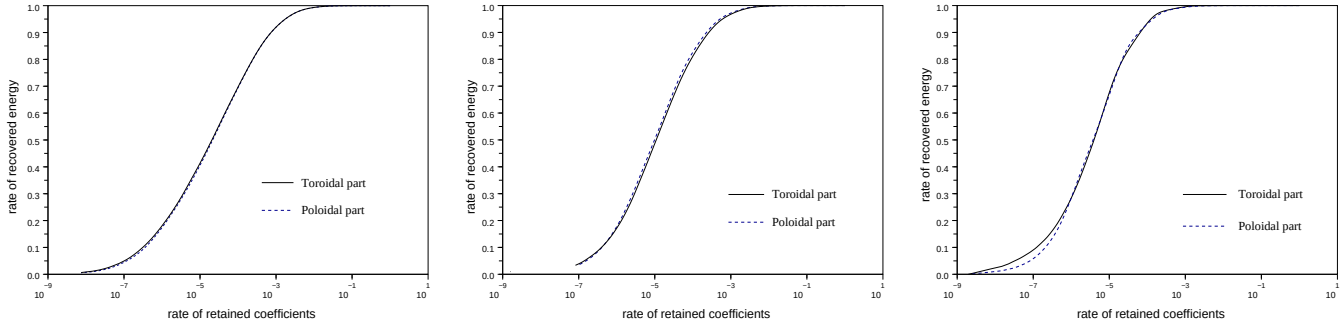

Figure 16: Compression curves for toroidal and poloidal parts of isotropic turbulence (left) rotating turbulence (middle) and stratified turbulence (right) done with isotropic orthogonal Crayalets.

the compression results are equivalent.

There are different perspectives of this work. The proposed Crayalets could be used to identify and to extract coherent vortices out of geophysical turbulence and to perform scale-dependent directional statistics to quantify their intermittency [34]. The projection

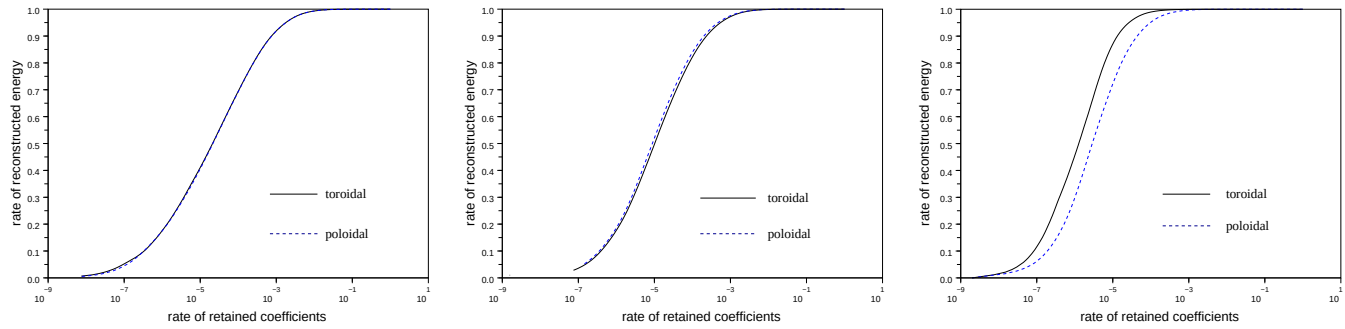

Figure 17: Compression curves for toroidal (in black) and poloidal (in blue) parts of isotropic turbulence (left) rotating turbulence (middle) and stratified turbulence (right) done with anisotropic orthogonal Craya wavelets.

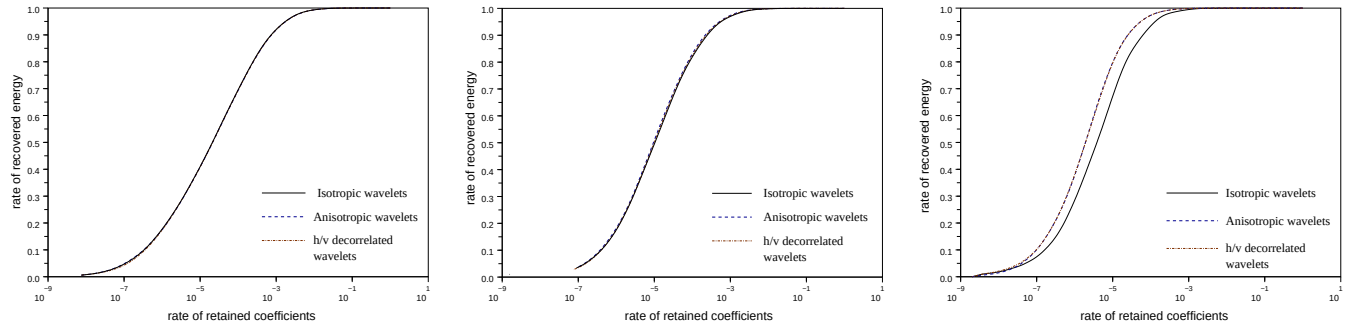

Figure 18: Compression curves with orthogonal Craya wavelets of different anisotropies for isotropic turbulence (left) rotating turbulence (middle) and stratified turbulence (right).

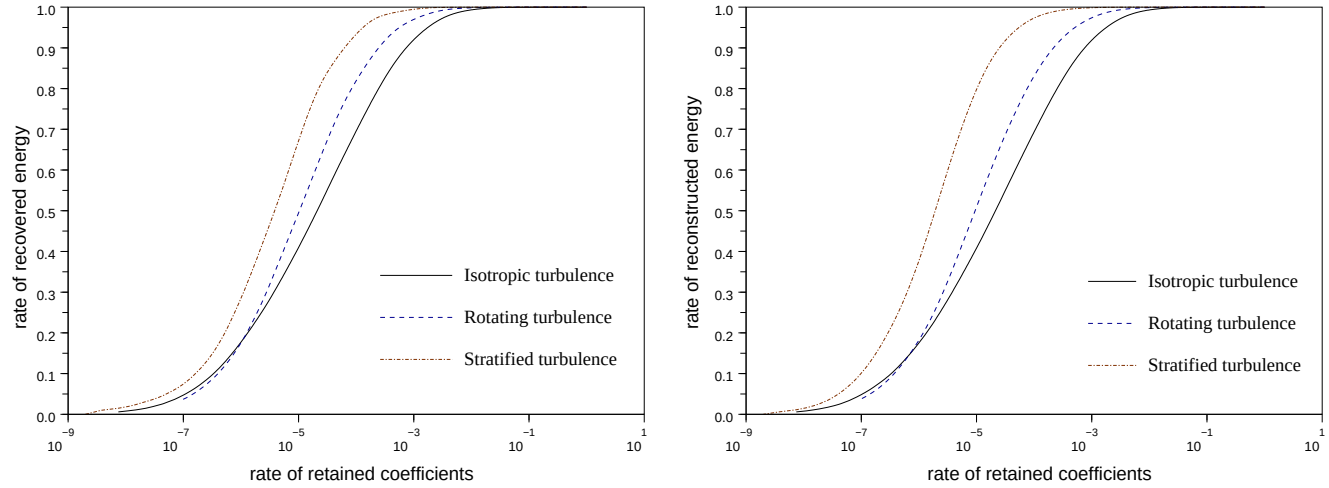

Figure 19: Compression curves for different turbulence (applied to the velocity fields), done with isotropic orthogonal Craya wavelets (left) and anisotropic orthogonal Craya wavelets (right).

of the Boussinesq equations onto a Crayalet basis yielding a dynamical system for the coefficients could be playground for modeling and for developing turbulence closures in wavelet space. Adaptive numerical discretizations using Crayalets for solving the Navier–

Stokes equations in the Boussinesq approximation are another promising direction for efficient numerical simulation of anisotropic turbulence.

Finally, let us mention, that the construction of vector-valued bases in higher space dimensions, satisfying incompressibility constraints and in addition yielding directional selectivity could be an interesting and effective representation of high dimensional anisotropic intermittent data encountered in data mining.

Acknowledgements

K.S. thanks Claude Cambon and Lukas Liechtenstein for fruitful discussion on the Craya decomposition and stratified turbulence and for providing his DNS data of rotating and stratified turbulence. We thank P.K Yeung for providing the DNS data of isotropic turbulence. The authors gratefully acknowledge financial support from the Agence Nationale de la Recherche, project M2TFP, contract N^o ANR-05-BLAN-0183-01. M.F. is grateful to the Wissenschaftskolleg zu Berlin for its hospitality.

References

[1] G. Battle and P. Federbush. Divergence-Free Vector Wavelets. *Michigan Math. J.*, **40**, 181–195, 1993.

[2] W.J.T. Bos, L. Liechtenstein and K. Schneider. Small scale intermittency in anisotropic turbulence. *Phys. Rev. E*, **76**, 046310, 2007.

[3] C. Cambon. Turbulence and vortex structures in rotating and stratified flows. *Eur. J. Mech. - B/Fluids*, **20**(4): 489–510, 2001.

[4] C. Cambon and L. Jacquin. Spectral approach to non-isotropic turbulence subjected to rotation. *J. Fluid Mech.*, **202**: 295–317, 1989.

[5] C. Cambon, C. Teissedre and D.C. Jeandel. Étude d'effets couplés de déformation et de rotation sur une turbulence homogène. *J. Méc. Théor. Appl.* **4**(5), 629–657, 1985.

[6] A. Craya. L'interprétation statistique de la turbulence, État de la question, *Revue de statistique appliquée*, **4**(2): 17–30, 1956.

[7] A. Craya. Contribution à l'analyse de la turbulence associée à des vitesses moyennes. *P.S.T. Ministère de l'air* (Paris), **345**, 1958.

[8] A. Craya and M. Darrigol. Turbulent swirling jet. *Phys. Fluids*, **10**(9), S197–S199, 1967.

[9] E. Deriaz and V. Perrier, Divergence-free wavelets in 2D and 3D, application to the Navier–Stokes equations. *J. Turbulence*, **7**(3), 2006.

[10] E. Deriaz, M. O. Domingues, V. Perrier, K. Schneider and M. Farge. Divergence-free wavelets for coherent vortex extraction in 3D homogeneous isotropic turbulence. *ESAIM: Proc.*, **16** 146–163, 2007.

[11] E. Deriaz and V. Perrier. Orthogonal Helmholtz decomposition in arbitrary dimension using divergence-free and curl-free wavelets. *Appl. Comput. Harmon. Anal.*, **26**(2), 249–269, 2009.

[12] M. Farge. Wavelet transforms and their application to turbulence. *Annu. Rev. Fluid Mech.*, **24**, 395–457, 1992.

[13] M. Farge, A. Azzalini, A. Mahalov, B. Nicolaenko, F. Tse, G. Pellegrino and K. Schneider. Vortex tubes in shear-stratified turbulence. *IUTAM Symposium on Tubes, Sheets and Singularities in Fluid Dynamics (Eds. C. Bajer and H.K. Moffatt)*, Kluwer Academic Publishers, 217–228, 2003.

[14] M. Farge and G. Rabreau. Transformée en ondelettes pour détecter et analyser les structures cohérentes dans les écoulements turbulents bidimensionnels. *C. R. Acad. Sci. Paris, Série II*, **307**, 1479–1486, 1988.

[15] F.S. Godeferd and C. Cambon, Detailed investigation of energy transfers in homogeneous stratified turbulence. *Phys. Fluids*, **6**, 2084, 1994,

[16] A. Grossmann and J. Morlet. Decomposition of Hardy functions into square integrable wavelets of constant shape. *SIAM J. Math. Anal.*, **15**, 723–736, 1984.

[17] J.R. Herring. Approach of axisymmetric turbulence to isotropy. *Phys. Fluids* **17**, 859–872, 1974.

[18] K. Kishida, K. Araki, S. Kishiba and K. Suzuki. Local or Nonlocal? Orthonormal divergence-free wavelet analysis of nonlinear interactions in turbulence. *Phys. Rev. Let.*, **83**(26), 5487–5490, 1999.

[19] K. Kishida, K. Araki. Orthogonal divergence-free wavelet analysis of spatial correlation between kinetic energy and nonlinear transfer in turbulence. *Statistical Theories and Computational Approaches to Turbulence, eds. Y. Kaneda and T. Gotoh*, Springer-Verlag Tokyo, 2002.

[20] P.G. Lemarié-Rieusset. Analyses multi-résolutions non orthogonales, commutation entre projecteurs et dérivation et ondelettes vecteurs à divergence nulle. *Revista Matemática Iberoamericana*, **8**(2), 221–236, 1992.

[21] P.G. Lemarié-Rieusset. Un théorème d'inexistence pour les ondelettes vecteurs à divergence nulle. *C. R. Acad. Sci. Paris, Série I*, **319**, 811–813, 1994.

[22] P.G. Lemarié-Rieusset. On the existence of compactly supported dual wavelets. *Appl. Comput. Harmon. Anal.*, **3**, 117–118, 1997.

[23] L. Liechtenstein. *Dynamique eulérienne et lagrangienne des écoulements turbulents stratifiés tournants.* PhD thesis, École Centrale de Lyon, 2005.

[24] L. Liechtenstein, F.S. Godeferd and C. Cambon. Nonlinear formation of structures in rotating stratified turbulence. *J. Turbul.*, **6**, 24, 2005.

[25] C. Meneveau. Analysis of turbulence in the orthonormal wavelet representation. *J. Fluid Mech.*, **232**, 469–520, 1991.

[26] J. Pedlosky. *Geophysical Fluid Dynamics.* Springer-Verlag, New York, 1979.

[27] J.J. Riley, R.W. Metcalfe and M.A. Weissman. Direct numerical simulations of homogeneous turbulence in density-stratified fluids. *AIP Conf. Proc.* **76**, 79, 1981.

[28] P. Sagaut and C. Cambon. *Homogeneous turbulence dynamics.* Cambridge University Press, 2008.

[29] K. Schneider and O. Vasilyev. Wavelet methods in computational fluid dynamics. *Annu. Rev. Fluid Mech.*, **42**, 473–503, 2010.

[30] K. Urban. On Divergence-free wavelets. *Adv. Comput. Math.* **4**(1,2), 51–82, 1995.

[31] K. Urban. Using divergence-free wavelets for the numerical solution of the Stokes problem. *AMLI'96: Proceedings of the Conference on Algebraic Multilevel Iteration Methods with Applications*, **2**: 261–277, University of Nijmegen, The Netherlands, 1996.

[32] F. Waleffe. The nature of triad interactions in homogeneous turbulence. *Phys. Fluids A*, **4**, 350, 1992.

[33] P. Yeung, D. Donzis and K. Sreenivasan. High Reynolds-number simulation of turbulent mixing. *Phys. Fluids*, **17**, 081703, 2005.

[34] K. Yoshimatsu, N. Okamoto, K. Schneider, Y. Kaneda and M. Farge. Intermittency and scale-dependent statistics in fully developed turbulence. *Phys. Rev. E*, **79**, 026303, 2009.